Contents lists available at ScienceDirect

Vacuum

journal homepage: www.elsevier.com/locate/vacuum

Electron–interface-phonon interaction strength in Pöschl–Teller quantum wells is enhanced considerably compared to rectangular ones

Luong Thi Huong [a], Tran Cong Phong [b,c], Le Ngoc Minh [d], Nguyen Dinh Hien [e,f,*]

[a] Nha Trang Central Ethnic Minority Pre-university, Nha Trang City, Khanh Hoa Province, Vietnam
[b] Atomic Molecular and Optical Physics Research Group, Institute for Advanced Study in Technology, Ton Duc Thang University, Ho Chi Minh City, Vietnam
[c] Faculty of Electrical and Electronics Engineering, Ton Duc Thang University, Ho Chi Minh City, Vietnam
[d] Faculty of Physics, University of Sciences, Hue University, Hue City, Vietnam
[e] Institute of Research and Development, Duy Tan University, Da Nang, Vietnam
[f] School of Engineering & Technology, Duy Tan University, Da Nang, Vietnam

ARTICLE INFO

ABSTRACT

We investigated the magneto-optical properties of the Pöschl–Teller GaAs/AlAs quantum well (QW) due to the electron–interface optical (IO) phonon interaction based on the optically-detected (OD) magneto–IO-phonon resonance (MIOPR) effect. The methods of the operator projection and the profile were used to calculate the MO-absorption power (MOAP) and measure the full width at half maximum (FWHM) of the OD-MIOPR peaks. The results are as follows: The well-width (L_W), the temperature of the electron–phonon system (T), and the magnetic field (B) strongly affect the MOAP and the FWHM of the OD-MIOPR peaks for both the two emission and absorption cases of IO-phonons in both the materials of the well and the barrier. The FWHMs in both the materials of the well and the barrier for the absorption case of an IO-phonon are bigger than those for the emission case. The FWHM due to IO-phonon interaction in the GaAs material of the well is stronger than that in the AlAs material of the barrier for both the two IO-phonons emission and absorption cases. Especially, the result also showed that the FWHMs in the Pöschl–Teller QW are always bigger than those in the rectangular QW for the two emission and absorption cases of IO-phonons in both the GaAs and AlAs materials of the well and the barrier, respectively. Our specific results are expected to be promising data for potential applications in optoelectronic devices.

1. Introduction

In recent years, there has been an increasing interest in studying semiconductor heterostructures, such as superlattice structures, inversion layers, quantum wells, and the like. The confined electronic states in such systems cause many new physical effects and properties with practical importance in micro- and optoelectronics device fabrication. Due to spatial separation from donor impurities, the mobility of a two-dimensional (2D) electron gas is significantly enhanced in heterostructure semiconductors at low temperatures. However, at high temperatures, electron interactions with optical phonons dominate the determination of various electronic properties, including mobility [1, 2]. 2D semiconductor structures are known to have unique properties and potential applications due to their high specific surface area [3], strong quantum confinement [4], and different electronic structures compared to bulk semiconductor structures [5–7]. Confining electrons in such nanostructures enhances radiative recombination efficiency, making them valuable for optoelectronic applications [8]. In recent

years, there has been an increasing interest in utilizing GaAs quantum wells that are embedded in AlAs/GaAs superlattices. This is because by replacing the AlGaAs alloy barriers with short-period superlattices, advanced microelectronic and optoelectronic devices such as quantum well lasers, LEDs, solar cells, photodetectors and micro-sensors, etc. can be produced with improved performance parameters [9,10]. Recently developed experimental techniques have revealed substantial atomic-scale roughness at GaAs/Al(Ga)As interfaces, including through chemical lattice mapping [11]. Various types of 2D materials possess distinctive features that make them practical for numerous applications such as bio-applications, topological spintronics, optoelectronics, electronics, and energy devices [12,13]. The optoelectronic properties of such materials change significantly when their thickness is reduced to a single or a few atomic layers, resulting in a shift from indirect to direct band-gap [14,15]. It is well known that phonon interaction plays a crucial role in the device physics of intersubband lasers based on QW structures. Through transitions of confined electrons between excited

---

conduction band states due to interaction by phonons, especially optical phonons localized in quantum wells, the physics of such intersubband laser devices generate photons. The above judgment for the role of optical phonons is particularly true for intersubband electron transitions due to their interaction in QW structures [16]. There has been significant interest in studying the issue of el–O-ph interaction in QW structures. In fact, there have been investigations of electron–optical-phonon interaction energies [17–19], the scattering rate [20–22], cyclotron resonance [23,24], the hot electron–optical phonon interactions [25], optical properties [26], magneto-optical properties [27–38], etc. In most of these works, the usual Fröhlich interaction based only on bulk and confined optical-phonons has been used. However, it was recognized recently that optical phonons in heterostructure semiconductors can be influenced strongly by the presence of heterointerfaces [39]. The present paper aims to elucidate the difference in the contributions of interface phonons to el–O-ph interactions between Pöschl–Teller and rectangular quantum wells. The unique features of the Pöschl–Teller potential lie in its tunable asymmetry, and the associated Schrödinger equation is solvable through the analytical method. The presence of heterointerfaces leads to optical phonon confinement in each layer and IO-phonons which are localized in the vicinity of interfaces. It has been theoretically demonstrated that in some cases, interface phonons can significantly contribute to the interaction between optic phonons and electrons [40]. There exist IO-phonons in heterostructure semiconductors that are localized in the vicinity of the interfaces and they have frequencies situated in the forbidden gap between transverse optical (TO) and longitudinal optical (LO) bulk phonons. It is well-known that at room temperature as well as higher temperatures, the el–IO-ph scattering mechanism can be considered to be a principal mechanism affecting electron transitions. A complete understanding of el–IO-ph scattering mechanisms and intensities is essential to further progress in nanodevice fields. In semiconductors containing polar materials such as gallium arsenide (GaAs), it is the optical phonons that exert a great influence on transport and optical properties. Therefore it is necessary to better understand el–O-ph interactions and optical phonon modes in heterostructures, particularly for IO-phonons and el–IO-ph interactions. GaAs is a vital semiconductor and is a compound of arsenic and gallium. It is used in a variety of applications, such as optoelectronic devices, infrared and laser diodes, solar cells, integrated circuits at microwave frequencies, light-emitting diodes, photovoltaic cells, thermoelectric devices, tunnel field-effect transistors, etc. In addition, GaAs has also been used in aerospace and military applications, like sensors, secure communications, and radars. There are two methods for producing GaAs nano-structures: by employing either top-down or bottom-up methods where various electrochemical etching techniques can be used for producing these structures. GaAs nanostructures come in various forms, including nano-wires and discs, quantum dots and wells, quantum rings and wires, nanopores, and so on. Electrochemically formed porous GaAs nano-structures are highly desirable for many various applications. Their distinct nanoscale characteristics and significant surface-to-volume ratio are the reasons for this. In addition, porous GaAs has a wide range of applications. It can be used as a virtual substrate for InGaAs, an anti-reflective coating for GaAs solar cells because of its low elasticity, and a temporary carrier for reducing solar cell weight through layer transfer processes. Porous GaAs has even been demonstrated to provide quick response to humidity sensing [41]. In the context of GaAs/AlAs quantum well, the inclusion of AlAs barriers results in the formation of GaAs/AlAs interfaces within the conducting channel. As the scattering rates due to IO-phonons are expected to rise with decreasing well width, it is crucial to ascertain the significance of IO-phonons as the well width varies. As a matter of fact, there are investigations have been conducted on the importance of IO-phonons in el–O-ph interaction and scattering such as polar IO-phonons in double heterostructures [40], in wurtzite nanocrystals [42], in wurtzite GaN/AlN QWs [43], in a wurtzite GaN-AlN nano-wire [44], in GaAs-AlAs superlattices [45], in quantum wells [46,47], in single and double heterostructures [2], and in GaN/ZnO heterostructures [16]. The investigation of el–IO-ph interaction in general and the optical absorption features in particular of heterostructure semiconductors has been of great interest from both applied and theoretical perspectives because of its crucial role in the production of optoelectronic devices. For single heterostructure semiconductors such as quantum wells, the problem of the contribution of the IO-phonons to el–O-ph interactions, we have also performed some works in very recent years as follows: the el–IO-ph scattering in QWs due to phonon absorption (emission) [48], the cyclotron–IO-phonon-resonance in semi-parabolic QWs [49], the influence of IO-phonons compared with confined phonons on cyclotron resonance in QWs [50], the contribution of various kinds of IO-phonons to the el–IO-ph scattering in two-dimensional electronic system [51], etc. Despite the extensive investigations conducted, the influence of IO-phonons on the el–O-ph interaction has not yet been elucidated fully in most of these studies because of various confining potential QWs that have not been considered. To date, there have not yet been detailed theoretical investigations on the el–IO-ph interaction in Pöschl–Teller and finite square potential QWs which are of great practical importance. Simultaneously, the effects of the quantum confinement potential of the electron on the strength of the el–IO-ph interaction have not yet been considered in the past years. Therefore a detailed investigation of the MO transition properties due to the el–IO-ph interaction for both two absorption and emission cases of an IO-phonons in the Pöschl–Teller QW structures is necessary to provide valuable insights into the production of optoelectronic devices and future experimental studies. In particular, the obtained result for the Pöschl–Teller QW was compared with that for the rectangular QW which has been previously published to elucidate the difference in the contributions of IO-phonons to el–O-ph interactions between two these two potential shapes. The comparative results obtained from the study may have significant consequences for practical device applications based on QW structures where the el–IO-ph interaction is one of the important mechanisms for carrier relaxation. In this paper, the MO-properties of the Pöschl–Teller GaAs-AlAs QW due to the el–IO-ph interaction for both the two absorption and emission cases of an IO-phonon in GaAs-well and AlAs-barrier materials based on the OD-MIOPR effect are studied. In particular, in addition to studying the crucial roles of IO-phonons for the MO-properties of the Pöschl–Teller GaAs/AlAs QW, we also try to elucidate the difference in the contributions of IO-phonons to el–O-ph interactions between Pöschl–Teller and rectangular QWs. In other words, the influence of the quantum confinement potential of electrons in QWs on the contributions of IO-phonons to el–ph interactions is also clarified in this work. In order to carry out this investigation, we will proceed with the following steps. First, we derive the confinement potential, the energy, and the wave function of the electron in the Pöschl–Teller QW. Second, we carry out accurate computations for the matrix element of the el–IO-ph interaction, in this case, IO-phonon modes play a very crucial role. Third, using the operator projection method in order to calculate accurately the MO conductivity tensor of the Pöschl–Teller QW electron due to the el–IO-ph interaction. Then, by inserting the MOCT expression into the MOAP one, and at the same time carrying out the systematic computations, we obtain the explicit expression for the MOAP due to the el–IO-ph interaction in the Pöschl–Teller QW. Finally, in order to complete this study, we utilize mathematical software to accurately numerically calculate and visually represent the physical graphs. The physical meaning of this work will be discussed in detail using analytical, numerical, and visual results. The outline of this paper is as follows. In Section 2, we present the potential Pöschl–Teller QW model, which includes the electron's confinement potential, energy, and wave function. More importantly, the IO-phonon modes and the matrix element of the el–IO-ph interaction in Pöschl–Teller QW are also presented in this section. In Section 3, we carry out accurate computations for the MOCT and the MOAP due to the el–IO-ph interaction in the Pöschl–Teller QW. Section 4 is the numerical results and discussion. Finally, Section 5 is the conclusion.

2. Electron–interface optical phonon interaction in Pöschl–Teller QWS

2.1. Pöschl–Teller QW model

We investigate a single Pöschl–Teller QW model that enables electrons to freely move in the (x, y) plane but are confined in the quantum-well growth direction (z-direction). Where the form of Pöschl–Teller confining potential is defined by [52–56]:

$$V(z) = \frac{\hbar^2\lambda^2}{2m^*}\left[\frac{\eta(\eta-1)}{\sin^2(\lambda z)} + \frac{\nu(\nu-1)}{\cos^2(\lambda z)}\right], \tag{1}$$

here $\lambda = \pi/(2L_W)$ in which L_W refers to the well-width, m^* represents the effective mass. The Pöschl–Teller potential, $V(z)$, can be adjusted for asymmetry utilizing parameters η and ν. Where if η is equal to ν, the confined potential, $V(z)$, of the electron in this QW becomes perfectly symmetrical. We study a Pöschl–Teller quantum system under a static, uniform magnetic field of strength B applied in the direction of growth of the QW. When employing the effective mass approximation, the eigenvalues of a single electron in the Pöschl–Teller QW and its eigenfunctions are expressed in a specific format as follows [54–56]:

$$\Psi_{\mathcal{N},m} = \frac{1}{\sqrt{L_y}}\psi_{\mathcal{N}}(x-x_0)e^{ik_y y}Y_m(z) \tag{2}$$

and

$$E_{\mathcal{N},m} = \left(\mathcal{N} + \frac{1}{2}\right)\hbar\omega_c + \frac{\lambda^2\hbar^2(\eta+\nu+2m)^2}{2m^*}. \tag{3}$$

Where, the subband and Landau indexes are represented respectively by m and $\mathcal{N}$, and they can take on values of $0, 1, 2$, etc. The quantities L_y and k_y are the well-width and the wave vector in the y-direction. The quantity $\psi_{\mathcal{N}}(x-x_0)$ is the harmonic oscillator function in which $x_0 = -r_c^2 k_y$ and $r_c = \hbar/\sqrt{m^*\varepsilon}$ denotes the cyclotron-radius, with $\varepsilon = \hbar e B/m^*$. The electronic wave-function in the QW growth direction, $Y_m(z)$, is given by [54–56]

$$\begin{aligned}Y_m(z) &= A_m\sin^\eta(\lambda z)\cos^\nu(\lambda z)\\ &\times {}_2F_1\left[-m, \eta+\nu+m, \eta+1/2; \sin^2(\lambda z)\right],\end{aligned} \tag{4}$$

here ${}_2F_1\left[-m, \eta+\nu+m, \eta+1/2; \sin^2(\lambda z)\right]$ is the hypergeometric function, and A_m the normalization constant. In Eq. (3), the cyclotron energy is represented by $\hbar\omega_c$ where $\hbar\omega_c = |e|B/(m^*c)$.

2.2. Matrix element of el–IO-ph interaction in Pöschl–Teller QW

The matrix element of the el–IO-ph interaction in GaAs/Al-As potential Pöschl–Teller QW is expressed in a specific format as follows [57, 58]

$$\begin{aligned}|\langle i|H_{el-IO-ph}|f\rangle|^2 &= \frac{2e^2\pi f_{\zeta\eta}\Omega}{S_0 q\hbar\omega_{\zeta\vartheta}(1\pm\Omega)}|\mathcal{F}_{mm'}^\zeta(q)|^2|J_{\mathcal{N},\mathcal{N}'}(\xi)|^2\\ &\times \delta_{k_\perp^f, k_\perp^i\pm q_\perp},\end{aligned} \tag{5}$$

here $S_0 = L_x L_y$, and $\omega_{\zeta\vartheta}$ the frequency of the IO-phonon modes, it takes the form

$$\omega_{\zeta\vartheta}^2 = $$
$$\frac{\chi_\zeta \pm [\chi_\zeta^2 - \hbar^4(\theta_{1\zeta}+\theta_{2\zeta})(\theta_{1\zeta}\omega_{LO1}^2\omega_{TO2}^2 - \theta_{2\zeta}\omega_{LO2}^2\omega_{TO1}^2)]^{1/2}}{\hbar^2(\theta_{1\zeta}+\theta_{2\zeta})}, \tag{6}$$

where the quantities such as χ_ζ, θ_{1s}, and θ_{1s} are described by the following expressions:

$$\chi_\zeta = \hbar^2[\theta_{1\zeta}(\omega_{TO2}^2+\omega_{LO1}^2) + \theta_{2\zeta}(\omega_{TO1}^2+\omega_{LO2}^2)]/2, \tag{7}$$

$$\theta_{1s} = \theta_{1\infty}(1-\Omega), \quad \theta_{2s} = \theta_{2\infty}(1+\Omega), \tag{8}$$

$$\theta_{1a} = \theta_{1\infty}(1+\Omega), \quad \theta_{2a} = \theta_{2\infty}(1-\Omega). \tag{9}$$

Where, the dielectric constants at high frequency are represented by $\theta_{1\infty}$ and $\theta_{2\infty}$ for the well GaAs-material and the barrier AlAs-material. Here, the subscripts 1 and 2 display the well GaAs-material and barrier AlAs-material. The two quantities Ω and $f_{\zeta\vartheta}$ in Eq. (5) take the form of

$$\Omega = \exp(-qL_W) \tag{10}$$

and

$$f_{\zeta\vartheta} = \frac{\hbar^2(\omega_{\zeta\vartheta}^2 - \omega_{TO1}^2)(\omega_{\zeta\vartheta}^2 - \omega_{TO2}^2)}{(\omega_{\zeta+}^2 - \omega_{\zeta-}^2)(\theta_{1\zeta}+\theta_{2\zeta})}, \tag{11}$$

here, q is the IO-phonon wave-vector, and the frequency of the LO- and TO-phonons in the well GaAs-material (barrier AlAs-material) which are represented by ω_{LO1} and ω_{TO1} (ω_{LO2} and ω_{TO2}). ζ reveals the symmetric (s) IO-phonon mode and antisymmetric (a) IO-phonon mode. $\vartheta = \pm$ is to distinguish between two IO-modes in the well GaAs-material (-) and the barrier AlAs-material (+). $\mathcal{F}_{mm'}^\zeta(q)$, in Eq. (5) denotes the overlap integral, is expressed in a specific format as follows

$$\mathcal{F}_{mm'}^\zeta(q) = \int_{-\infty}^\infty Y_m^*(z)[e^{qz} \pm e^{-qz}]Y_m(z)dz, \tag{12}$$

and $J_{\mathcal{N},\mathcal{N}'}(\xi)$ is a quantity which is given by

$$|J_{\mathcal{N},\mathcal{N}'}(\xi)|^2 = \frac{N_2!e^{-\xi}\xi^{N_1-N_2}}{N_1!}[L_{N_2}^{N_1-N_2}(\xi)]^2, \tag{13}$$

with $\xi = r_c^2 q^2/2$, $N_1 = max\{\mathcal{N}, \mathcal{N}'\}$, $N_2 = min\{\mathcal{N}, \mathcal{N}'\}$, and $L_{N_2}^{N_1-N_2}(\xi)$ is the Laguerre polynomial.

3. Conductivity tensor and absorption power

3.1. MO-conductivity tensor produced by el–IO-ph interaction in Pöschl-Teller QW

When a circularly polarized electromagnetic wave is incident upon a quantum system with angular frequency ω, the MOCT of the electrons produced by el–IO-ph interaction in Pöschl–Teller QW is represented by [59–62]

$$\mathcal{K}_{+-}(\omega) = \frac{i}{\omega}\lim_{\Delta\to 0^+}\sum_\gamma (j_\gamma^+)^* T_R\{\rho_0(H)[\mathcal{X}, c_\gamma^\dagger c_{\gamma+1}]\}, \tag{14}$$

where the value of j_γ^+ can be determined by using the formula $j_\gamma^+ = -ie[2(\mathcal{N}_\gamma + 1)\hbar\omega_c/m^*]^{1/2}$. The many-body trace is represented by T_R, while the grand canonical density operator is denoted by $\rho_0(H)$. The operator c_γ^+ ($c_{\gamma+1}$) is utilized for both electronic creating (annihilating) in the $|\gamma\rangle$ ($|\gamma+1\rangle$) state within the Pöschl–Teller QW. The operator $\mathcal{X}$ is defined by $\mathcal{X} = (\hbar\bar\omega - \mathcal{L})^{-1}\mathcal{J}_+$, where $\mathcal{J}_+ = \mathcal{J}_x + i\mathcal{J}_y$ the current density operator, and $\mathcal{L}$ the Liouville operator. Calculating further the MOCT of electrons in the Pöschl–Teller QW can be achieved through the projection operators which are defined as

$$P_\gamma\mathcal{X} = \frac{\langle\mathcal{X}\rangle_\gamma}{\langle\mathcal{J}_+\rangle_\gamma}\mathcal{J}_+ \quad \text{and} \quad Q_\gamma = 1 - P_\gamma, \tag{15}$$

here

$$\langle\mathcal{X}\rangle_\gamma = T_R\{\rho_0(H)[\mathcal{X}, c_\gamma^\dagger c_{\gamma+1}]\}. \tag{16}$$

Applying the relation, $P_\gamma + Q_\gamma = 1$, on the right hand side of the Liouville operator $\mathcal{L}$, and at the same time utilizing the identity (AB) which is determined by the expression $(A-B)^{-1} = A^{-1} + A^{-1}B(A-B)^{-1}$ and $\langle\mathcal{J}_+\rangle_\gamma = j_{\gamma+1}^+(f_{\gamma+1} - f_\gamma)$ in calculation, we finally possess the precise representation of the MOCT produced by el–IO-ph interaction in the Pöschl–Teller QW, as shown below:

$$\mathcal{K}_{+-}(\omega) = \frac{i}{\hbar\omega}\lim_{\Delta\to 0^+}\sum_\gamma \frac{|j_\gamma^+|^2(f_{\gamma+1} - f_\gamma)}{\bar\omega - \omega_c - \mathcal{G}_\gamma(\bar\omega)}, \tag{17}$$

here the Fermi–Dirac distribution function is represented by $f_\gamma = 1/\{\exp[(E_\gamma - E_F)/k_B T] + 1\}$ in which E_F refers to the Fermi level, and the line-width function by $\mathcal{G}_\gamma(\bar\omega)$ which takes the form

$$
\begin{aligned}
\mathcal{G}_\gamma(\bar\omega) &= \frac{1}{\hbar(f_{\gamma+1} - f_\gamma)} \sum_\mu \sum_q |C_{\gamma,\mu}(q)|^2 \\
&\times \left[\frac{(1+\varrho_q)f_{\gamma+1}(1-f_\mu)}{\hbar\bar\omega + \hbar\omega_{\zeta\vartheta} - \mathcal{E}_{\gamma+1,\mu}} - \frac{\varrho_q f_\mu(1-f_{\gamma+1})}{\hbar\bar\omega + \hbar\omega_{\zeta\vartheta} - \mathcal{E}_{\gamma+1,\mu}} \right. \\
&\left. - \frac{(1+\varrho_q)f_\mu(1-f_{\gamma+1})}{\hbar\bar\omega - \hbar\omega_{\zeta\vartheta} - \mathcal{E}_{\gamma+1,\mu}} + \frac{\varrho_q f_{\gamma+1}(1-f_\mu)}{\hbar\bar\omega - \hbar\omega_{\zeta\vartheta} - \mathcal{E}_{\gamma+1,\mu}} \right] \\
&+ \frac{1}{\hbar(f_{\gamma+1} - f_\gamma)} \sum_\mu \sum_q |C_{\mu,\gamma+1}(q)|^2 \\
&\times \left[\frac{(1+\varrho_q)f_\mu(1-f_\gamma)}{\hbar\bar\omega + \hbar\omega_{\zeta\vartheta} - \mathcal{E}_{\mu\gamma}} - \frac{\varrho_q f_\gamma(1-f_\mu)}{\hbar\bar\omega + \hbar\omega_{\zeta\vartheta} - \mathcal{E}_{\mu\gamma}} \right. \\
&\left. - \frac{(1+\varrho_q)f_\gamma(1-f_\mu)}{\hbar\bar\omega - \hbar\omega_{\zeta\vartheta} - \mathcal{E}_{\mu\gamma}} + \frac{\varrho_q f_\mu(1-f_\gamma)}{\hbar\bar\omega - \hbar\omega_{\zeta\vartheta} - \mathcal{E}_{\mu\gamma}} \right].
\end{aligned}
\tag{18}
$$

In Eq. (18), $C_{\gamma,\mu}(q)$ and $C_{\mu,\gamma+1}(q)$ is the matrix-elements of the el–IO-ph interaction in QW, they take the form, $C_{\gamma,\mu}(q) = V_q\langle\gamma|e^{i\mathbf{q}.\mathbf{r}}|\mu\rangle$ and $C_{\mu,\gamma+1}(q) = V_q\langle\mu|e^{i\mathbf{q}.\mathbf{r}}|\gamma+1\rangle$, in which the symbol V_q represents the el–IO-ph coupling factor, while $\mathbf{r}$ the electronic position vector. $\mathcal{E}_{\mu\gamma}$ is discrepancy in electronic energy between two $|\mu\rangle$ and $|\gamma\rangle$ states, $\hbar\omega_{\zeta\vartheta}$ the IO-phonon energy, and $\varrho_q = [\exp(\hbar\omega_{\zeta\vartheta}/k_B T) - 1]^{-1}$ the Planck distribution function for the IO-mode in the Pöschl–Teller QW.

3.2. MO-absorption power produced by el–IO-ph interaction in Pöschl-Teller QW

The formula for the average MO-absorption power of the electron due to el–IO-ph interaction per unit volume for the Pöschl–Teller QW produced by an electromagnetic wave, is represented by [61,62]

$$
P(\omega) = \frac{E_0^2}{2} Re\{\mathcal{K}_{+-}(\omega)\},
\tag{19}
$$

where E_0 is the electrical-field amplitude, $Re\{\mathcal{K}_{+-}(\omega)\}$ represents the real part of the MOCT produced by el–IO-ph interaction per unit volume of the potential Pöschl–Teller QW.

In order to obtain the precise representation of the MO-absorption power produced by el–IO-ph interaction in the Pöschl–Teller QW, we now have to proceed with systematic computations for $Re\{\mathcal{K}_{+-}(\omega)\}$ in Eq. (19). In Eq. (17), we have $\bar\omega = \omega - i\Delta$ in which $\Delta \to 0^+$. This results in $\mathcal{G}_\gamma(\bar\omega)$ being a complex quantity, and hence it can be developed under the following form

$$
\mathcal{G}_\gamma(\bar\omega) = \mathcal{H}_\gamma(\omega) + i\mathcal{M}_\gamma(\omega),
\tag{20}
$$

here, $\mathcal{H}_\gamma(\omega)$ and $\mathcal{M}_\gamma(\omega)$ represent the line-shift and the line-width, respectively. To achieve the objectives mentioned in the Introduction of this study, we focus on calculation for the line-width, $\mathcal{M}_\gamma(\omega)$. On the other hand, in comparison to ω_c, the term $\mathcal{H}_\gamma(\omega)$ can be left out in the extreme quantum limit. Utilizing the Dirac identity takes the form $\lim_{\Delta\to 0^+}[1/(x - i\Delta)] = p(1/x) + i\pi\delta(x)$ and Eq. (20), once the calculation process is complete, we are left with the result for $\mathcal{M}_\gamma(\omega)$ is as follows:

$$
\begin{aligned}
\mathcal{M}_\gamma(\omega) &= \frac{\pi}{\hbar(f_{\gamma+1} - f_\gamma)} \sum_\mu \sum_q |C_{\gamma,\mu}(q)|^2 \\
&\times \left[(1+\varrho_q)f_{\gamma+1}(1-f_\mu)\delta(Z_1^+) - \varrho_q f_\mu(1-f_{\gamma+1})\delta(Z_1^+) \right. \\
&\left. - (1+\varrho_q)f_\mu(1-f_{\gamma+1})\delta(Z_1^-) + \varrho_q f_{\gamma+1}(1-f_\mu)\delta(Z_1^-) \right] \\
&+ \frac{\pi}{\hbar(f_{\gamma+1} - f_\gamma)} \sum_\mu \sum_q |C_{\mu,\gamma+1}(q)|^2 \\
&\times \left[(1+\varrho_q)f_\mu(1-f_\gamma)\delta(Z_2^+) - \varrho_q f_\gamma(1-f_\mu)\delta(Z_2^+) \right. \\
&\left. - (1+\varrho_q)f_\gamma(1-f_\mu)\delta(Z_2^-) + \varrho_q f_\mu(1-f_\gamma)\delta(Z_2^-) \right],
\end{aligned}
\tag{21}
$$

where $Z_1^\pm$ and $Z_2^\pm$ are given by

$$
Z_1^\pm = \hbar\omega \pm \hbar\omega_{\zeta\vartheta} - \mathcal{E}_{\gamma+1,\mu}
\tag{22}
$$

and

$$
Z_2^\pm = \hbar\omega \pm \hbar\omega_{\zeta\vartheta} - \mathcal{E}_{\mu\gamma}.
\tag{23}
$$

Using the two Eqs. (17) and (20), we obtain

$$
\begin{aligned}
\mathcal{K}_{+-}(\omega) &= \frac{1}{\hbar\omega} \sum_\gamma |j_\gamma^+|^2 \frac{(f_\gamma - f_{\gamma+1})\mathcal{M}_\gamma(\omega)}{(\omega - \omega_c)^2 + [\mathcal{M}_\gamma(\omega)]^2} \\
&+ i|j_\gamma^+|^2 \frac{(f_{\gamma+1} - f_\gamma)(\omega - \omega_c)}{(\omega - \omega_c)^2 + [\mathcal{M}_\gamma(\omega)]^2}.
\end{aligned}
\tag{24}
$$

After carrying out the development steps, we get $Re\{\mathcal{K}_{+-}(\omega)\}$ of the MOCT produced by el–IO-ph interaction in the potential Pöschl–Teller QW as:

$$
Re\{\mathcal{K}_{+-}(\omega)\} = \frac{1}{\hbar\omega} \sum_\gamma \frac{|j_\gamma^+|^2(f_\gamma - f_{\gamma+1})\mathcal{M}_\gamma(\omega)}{(\omega - \omega_c)^2 + [\mathcal{M}_\gamma(\omega)]^2}.
\tag{25}
$$

By inserting Eq. (25) into Eq. (19), the expression for photon frequency (ω) dependence of the average MOAP of the electron per unit volume for the Pöschl–Teller QW produced by el–IO-ph interaction, is obtained as

$$
P(\omega) = \frac{E_0^2}{2\hbar\omega} \sum_\gamma \frac{|j_\gamma^+|^2(f_\gamma - f_{\gamma+1})\mathcal{M}_\gamma(\omega)}{(\omega - \omega_c)^2 + [\mathcal{M}_\gamma(\omega)]^2}.
\tag{26}
$$

Finally, in order to achieve the explicit representation of the MOAP, $P(\omega)$, in Eq. (26) produced by the el–IO-ph interaction in the potential Pöschl–Teller QW, we now have to proceed with systematic computations for the matrix-elements $|C_{\gamma,\mu}(q)|^2$ and $|C_{\mu,\gamma+1}(q)|^2$ in Eq. (21) by making use of the relations are given by

$$
\begin{aligned}
\sum_\mu \cdots &\to \sum_{\mathcal{N}} \sum_m \cdots, \\
\sum_q \cdots &\to \frac{S_0 L_W}{4\pi^2} \int_0^\infty q_\perp dq_\perp \int_{-\infty}^\infty dq_z \cdots.
\end{aligned}
\tag{27}
$$

Once the systematic calculation process is complete, we are left with the final result for the line-width function of the absorption spectrum, $\mathcal{M}_\gamma(\omega)$, as follows:

$$
\begin{aligned}
\mathcal{M}_\gamma(\omega) &= \frac{e^2}{16\hbar^2\pi} \sum_{\mathcal{N}'} \sum_{m'} \sum_{\vartheta=\pm} \frac{1}{(f_{\mathcal{N}+1,m} - f_{\mathcal{N},m})} \\
&\times \int_0^\infty dq \frac{f_{\zeta\vartheta}}{\omega_{\zeta\vartheta}} \Omega(1\pm\Omega)^{-1} |\mathcal{F}_{m'm}^\zeta(q)|^2 |J_{\mathcal{N},\mathcal{N}'}(\xi)|^2 \\
&\times \left[\left(1+\varrho_q(\omega_{\zeta\vartheta})\right) f_{\mathcal{N}+1,m}(1-f_{\mathcal{N}',m'})\delta(\mathfrak{R}_1^+) \right. \\
&- \varrho_q(\omega_{\zeta\vartheta})f_{\mathcal{N}',m'}(1-f_{\mathcal{N}+1,m})\delta(\mathfrak{R}_1^+) \\
&- (1+\varrho_q(\omega_{\zeta\vartheta}))f_{\mathcal{N}',m'}(1-f_{\mathcal{N}+1,m})\delta(\mathfrak{R}_1^-) \\
&\left. + \varrho_q(\omega_{\zeta\vartheta})f_{\mathcal{N}+1,m}(1-f_{\mathcal{N}',m'})\delta(\mathfrak{R}_1^-) \right] \\
&+ \frac{e^2}{16\hbar^2\pi} \sum_{\mathcal{N}'} \sum_{m'} \sum_{\vartheta=\pm} \frac{1}{(f_{\mathcal{N}+1,m} - f_{\mathcal{N},m})} \\
&\times \int_0^\infty dq \frac{f_{\zeta\vartheta}}{\omega_{\zeta\vartheta}} \Omega(1\pm\Omega)^{-1} |\mathcal{F}_{m'm}^\zeta(q)|^2 |J_{\mathcal{N}+1,\mathcal{N}'}(\xi)|^2 \\
&\times \left[\left(1+\varrho_q(\omega_{\zeta\vartheta})\right) f_{\mathcal{N}',m'}(1-f_{\mathcal{N},m})\delta(\mathfrak{R}_2^+) \right. \\
&- \varrho_q(\omega_{\zeta\vartheta})f_{\mathcal{N},m}(1-f_{\mathcal{N}',m'})\delta(\mathfrak{R}_2^+) \\
&- \left(1+\varrho_q(\omega_{\zeta\vartheta})\right)f_{\mathcal{N},m}(1-f_{\mathcal{N}',m'})\delta(\mathfrak{R}_2^-) \\
&\left. + \varrho_q(\omega_{\zeta\vartheta})f_{\mathcal{N}',m'}(1-f_{\mathcal{N},m})\delta(\mathfrak{R}_2^-) \right],
\end{aligned}
\tag{28}
$$

where $\mathfrak{R}_1^\pm$ and $\mathfrak{R}_2^\pm$ are given by the two equations as below:

$$
\begin{aligned}
\mathfrak{R}_1^\pm = \hbar\omega &- (\mathcal{N}+1-\mathcal{N}')\hbar\omega_c \pm \hbar\omega_{\zeta\vartheta} \\
&- \frac{\lambda^2\hbar^2}{2m^*}\left[(\eta+\nu+2m)^2 - (\eta+\nu+2m')^2\right]
\end{aligned}
\tag{29}
$$

and

$$
\begin{aligned}
\mathfrak{R}_2^\pm = \hbar\omega &- (\mathcal{N}'-\mathcal{N})\hbar\omega_c \pm \hbar\omega_{\zeta\vartheta} \\
&- \frac{\lambda^2\hbar^2}{2m^*}\left[(\eta+\nu+2m')^2 - (\eta+\nu+2m)^2\right].
\end{aligned}
\tag{30}
$$

We use Lorentzian widths $Y_{\mathcal{N},\mathcal{N}'}$ and $Y_{\mathcal{N}+1,\mathcal{N}'}$ instead of Dirac delta functions in our calculation for Eq. (28). Two equations describe the widths are [63]:

$$\delta(\mathfrak{R}_1^\pm) = \frac{1}{\pi} \frac{\Theta_{\mathcal{N},\mathcal{N}'}^\pm}{(\mathfrak{R}_1^\pm)^2 + (\Theta_{\mathcal{N},\mathcal{N}'}^\pm)^2} \quad (31)$$

and

$$\delta(\mathfrak{R}_2^\pm) = \frac{1}{\pi} \frac{\Theta_{\mathcal{N}+1,\mathcal{N}'}^\pm}{(\mathfrak{R}_1^\pm)^2 + (\Theta_{\mathcal{N}+1,\mathcal{N}'}^\pm)^2}, \quad (32)$$

where the Lorentzian widths $\Theta_{\mathcal{N},\mathcal{N}'}$ and $\Theta_{\mathcal{N}+1,\mathcal{N}'}$ are determined by

$$\left(\Theta_{\mathcal{N}',\mathcal{N}}^\pm\right)^2 = \frac{e^2}{2\pi\hbar L_W} \sum_{\vartheta=\pm} \int_0^\infty dq \frac{f_{\zeta\vartheta}}{\omega_{\zeta\vartheta}} \left[\varrho_q(\omega_{\zeta\vartheta}) + \frac{1}{2} \pm \frac{1}{2}\right] \quad (33)$$
$$\times \Omega(1\pm\Omega)^{-1}|\mathcal{F}_{m'm}^\zeta(q)|^2 |J_{\mathcal{N},\mathcal{N}'}(\xi)|^2,$$

$$\left(\Theta_{\mathcal{N}+1,\mathcal{N}'}^\pm\right)^2 = \frac{e^2}{2\pi\hbar L_W} \sum_{\vartheta=\pm} \int_0^\infty dq \frac{f_{\zeta\vartheta}}{\omega_{\zeta\vartheta}} \left[\varrho_q(\omega_{\zeta\vartheta}) + \frac{1}{2} \pm \frac{1}{2}\right] \quad (34)$$
$$\times \Omega(1\pm\Omega)^{-1}|\mathcal{F}_{m'm}^\zeta(q)|^2 |J_{\mathcal{N}+1,\mathcal{N}'}(\xi)|^2.$$

Finally, the calculation of the overlap integral, $\mathcal{F}_{m'm}^\zeta(q)$, is precise and can be done as follows. By using the two Eqs. (4) and (12), and setting $t = \lambda z \Rightarrow dz = dt/\lambda$, with $0 \le t \le \lambda L_W$, we have

$$\mathcal{F}_{mm'}^\zeta(q) = \quad (35)$$
$$\frac{1}{\lambda} \int_0^{\lambda L_W} Y_{m'}^* \left(\frac{t}{\lambda}\right) \left[\exp\left(\frac{q}{\lambda}t\right) \pm \exp\left(-\frac{q}{\lambda}t\right)\right] Y_m \left(\frac{t}{\lambda}\right) dt.$$

After completing the systematic calculation process, we obtain the final result for the overlap integral represented by the two expressions $\mathcal{F}_{mm'}^{\zeta+}(q)$ and $\mathcal{F}_{mm'}^{\zeta-}(q)$ as below:

$$\mathcal{F}_{mm'}^{\zeta+}(q) = \frac{2A_m A_{m'}}{\lambda} \int_0^{\lambda L_W} dt \sin^{2\eta}(t) \cos^{2\nu}(t) \cosh\left(\frac{q}{\lambda}t\right)$$
$$\times {}_2F_1\left[-m, \eta + \nu + m, \eta + \frac{1}{2}, \sin^2(t)\right] \quad (36)$$
$$\times {}_2F_1\left[-m', \eta + \nu + m', \eta + \frac{1}{2}, \sin^2(t)\right]$$

and

$$\mathcal{F}_{mm'}^{\zeta-}(q) = \frac{2A_m A_{m'}}{\lambda} \int_0^{\lambda L_W} dt \sin^{2\eta}(t) \cos^{2\nu}(t) \sinh\left(\frac{q}{\lambda}t\right)$$
$$\times {}_2F_1\left[-m, \eta + \nu + m, \eta + \frac{1}{2}, \sin^2(t)\right] \quad (37)$$
$$\times {}_2F_1\left[-m', \eta + \nu + m', \eta + \frac{1}{2}, \sin^2(t)\right],$$

where $A_m = 1/\sqrt{J_m}$, with J_m is determined by

$$J_m = \frac{1}{\lambda} \int_0^{\lambda L_W} \sin^{2\eta}(t) \cos^{2\nu}(t)$$
$$\times {}_2F_1\left[-m, \eta + \nu + m, \eta + \frac{1}{2}, \sin^2(t)\right]^2 dt. \quad (38)$$

Here, the values of the overlap integrals, $\mathcal{F}_{mm'}^{\zeta+}(q)$ and $\mathcal{F}_{mm'}^{\zeta-}(q)$, in Eqs. (36) and (37) produced by the el–IO-ph interaction in the Pöschl–Teller QW are obtained by numerical calculations. Based on analytical findings, we employ precise computational techniques to conduct numerical calculations on GaAs/AlAs material. The reliable results of the graphical representations produced by the el–IO-ph interaction in the Pöschl–Teller QW are obtained. The physical conclusions of this study are in the next section.

4. Numerical results and discussion

To clarify the difference in the MO-properties which produced by the el–IO-ph interaction between the Pöschl–Teller and rectangular GaAs/AlAs QWs in both the two absorption and emission cases of an IO-phonon in the well and barrier, numerical calculations on the GaAs-well and AlAs-barrier materials were proceeded in this investigation and obtained the important results as below. Where the parameters of the GaAs-well and AlAs-barrier materials utilized [58,64]: $\hbar\omega_{TO1}$ and
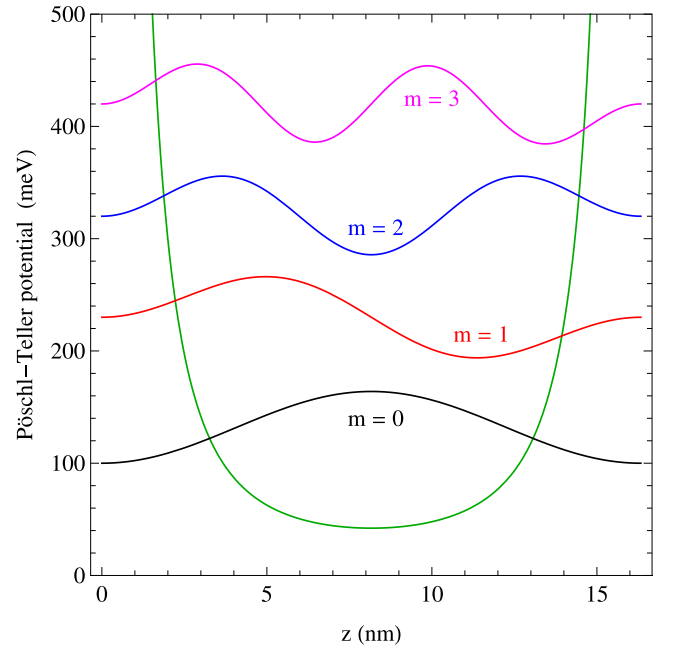

Fig. 1. The four wave-functions of the Pöschl–Teller confinement electron at $L_W = \sqrt{\frac{5}{3}} \times 12.65 \times 10^{-9}$ m and $\eta = \nu = 2$ for the ground state ($m = 0$), and the three excited states include: first ($m = 1$), second ($m = 2$), and third ($m = 3$) excited states.
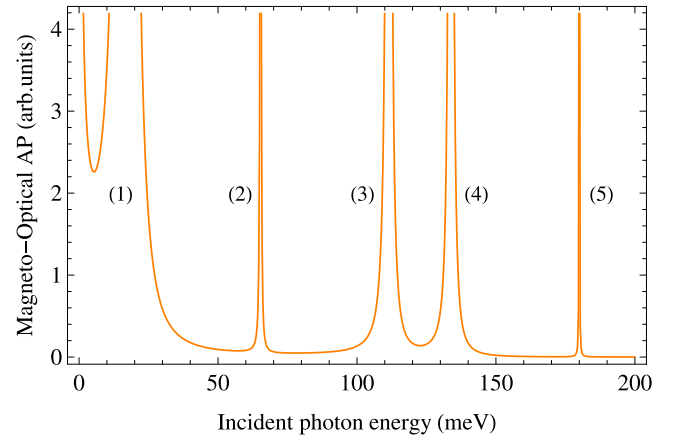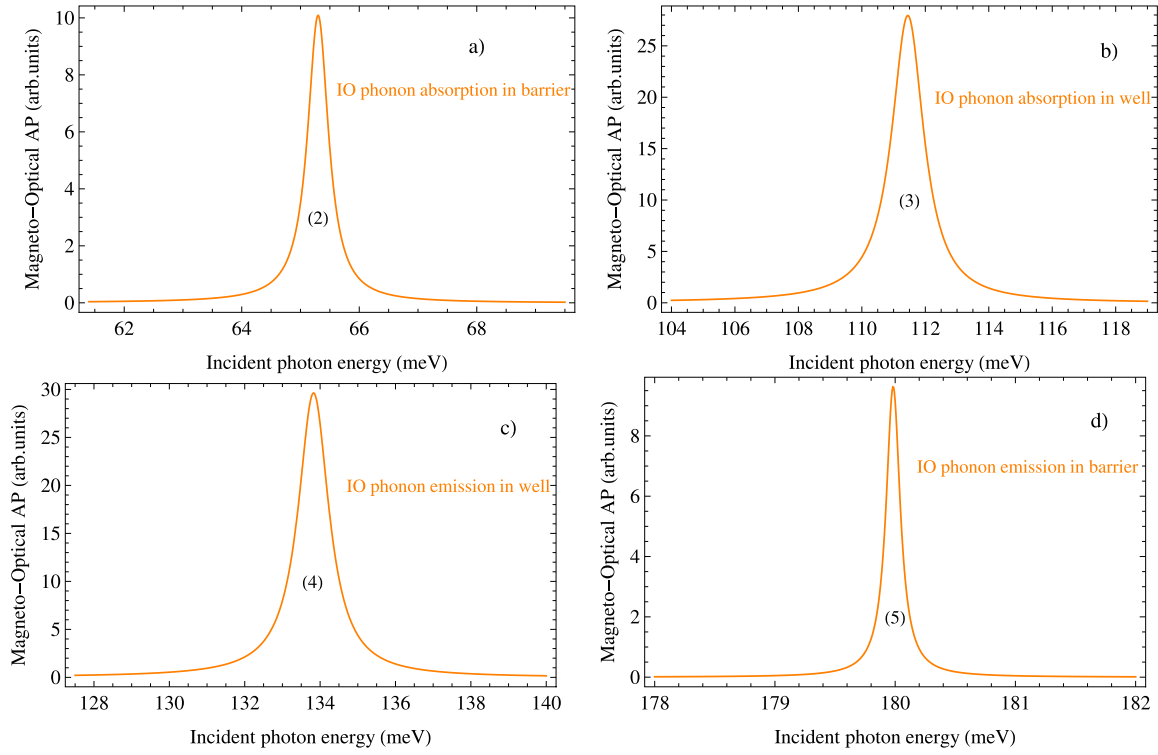

Fig. 2. Photon-energy ($\hbar\omega$) dependent MOAP due to the el–IO-ph interaction in both the well and barrier of the Pöschl–Teller GaAs/AlAs QW at $B = 10$ T, $L_W = \sqrt{\frac{5}{3}} \times 12.65 \times 10^{-9}$ m, $\eta = \nu = 2$, and $T = 300$ K.

$\hbar\omega_{TO2}$ of 33.29 meV and 44.28 meV; $\hbar\omega_{LO1}$ and $\hbar\omega_{LO2}$ of 36.25 meV and 50.09 meV; $\theta_{1\infty}$ and $\theta_{2\infty}$ of 10.89 and 8.16, respectively; $E_0 = 5.0 \times 10^6$ V/m and $m^* = 0.067m_0$ (m_0 is the free electronic mass). Assuming that $m = 0; m' = 0, 1$ and $\mathcal{N} = 0, \mathcal{N}' = 1$ are occupied by quantum-well electrons.

In Fig. 1, we plotted the four wave-functions of the Pöschl–Teller confinement electron at $L_W = \sqrt{\frac{5}{3}} \times 12.65 \times 10^{-9}$ m and $\eta = \nu = 2$ for the ground state ($m = 0$), and the three excited states include: first ($m = 1$), second ($m = 2$), and third ($m = 3$) excited states. From the plot, it can be obviously seen that at the value $\eta = \nu = 2$, the profile of the Pöschl–Teller electronic potential perfectly is symmetrical at the position $\lambda z = \pi/4$. The obtained profiles of the four wave-functions of the Pöschl–Teller confinement electron are evident and relatively reasonable.

In Fig. 2, we plotted the photon-energy ($\hbar\omega$) dependent MOAP due to the el–IO-ph interaction in both the GaAs-well and AlAs-barrier of

Fig. 3. Photon-energy dependent MOAP due to the el–IO-ph interaction at the four OD-MIOPR peaks in the two emission and absorption cases of an IO-phonon in the well GaAs-material (Figs. 3(b) and 3(c)) and barrier AlAs-material (Figs. 3(a) and 3(d)) of the Pöschl–Teller GaAs/AlAs QW. Where $B = 10$ T, $L_W = \sqrt{\frac{5}{3}} \times 12.65 \times 10^{-9}$ m, $\eta = \nu = 2$, and $T = 300$ K.

the Pöschl–Teller GaAs/AlAs QW at $B = 10$ T, $L_W = \sqrt{\frac{5}{3}} \times 12.65 \times 10^{-9}$ m, $T = 300$ K, and $\eta = \nu = 2$. From the obtained plot, we see that it clearly appeared the five resonant peaks are numbered from (1)-number to (5)-number and described as follows: The (1)-number peak is shown in the above plot as the cyclotron resonance (CR) peak is caused by satisfying the condition of the CR, $\hbar\omega = \hbar\omega_C$, i.e., $\hbar\omega_1 = 17.287$ (meV). Furthermore, the (2) and- (5)-number peaks are shown in the above plot as the two OD-MIOPR peaks in the two absorption ((2)-number peak) and emission ((5)-number peak) cases of an IO-phonon in the AlAs-barrier material of the Pöschl–Teller GaAs/AlAs QW are caused by corresponding satisfying the two conditions of the two OD-MIOPRs are that $\hbar\omega = (\mathcal{N}_2 - \mathcal{N}_1)\hbar\omega_C - \varepsilon_0[(\eta + \nu + 2m_1)^2 - (\eta + \nu + 2m_2)^2] - \hbar\omega_{IO-B}$ and $\hbar\omega = (\mathcal{N}_2 - \mathcal{N}_1)\hbar\omega_C - \varepsilon_0[(\eta + \nu + 2m_1)^2 - (\eta + \nu + 2m_2)^2] + \hbar\omega_{IO-B}$, i.e., $\hbar\omega_2$ and $\hbar\omega_5$ of 65.300 (meV) and 179.983 (meV). Where $\varepsilon_0 = (\pi\hbar)^2/(8m^*L_W^2)$. Here, the (2)-number OD-MIOPR peak describes the simultaneous absorption of the energies of an IO-phonon in the AlAs-barrier material ($\hbar\omega_{IO-B}$) and of an incident photon ($\hbar\omega$) by the Pöschl–Teller potential confinement electron to shift from $\mathcal{N}_1$ to $\mathcal{N}_2$ and m_1 to m_2 in the Pöschl–Teller GaAs/AlAs QW. The (5)-number OD-MIOPR peak describes in detail the emission of the energy of an IO-phonon in the AlAs-barrier material ($\hbar\omega_{IO-B}$) and the absorption of an incident photon ($\hbar\omega$) by the Pöschl–Teller potential confinement electron to shift from $\mathcal{N}_1$ to $\mathcal{N}_2$ and m_1 to m_2 in the Pöschl–Teller GaAs/AlAs QW. Finally, the (3) and- (4)-number peaks are shown in the above plot as the two OD-MIOPR peaks in the two absorption ((3)-number peak) and emission ((4)-number peak) cases of an IO-phonon in the GaAs-well material of the Pöschl–Teller GaAs/AlAs QW are caused by corresponding satisfying the two conditions of the two OD-MIOPRs are that $\hbar\omega = (\mathcal{N}_2 - \mathcal{N}_1)\hbar\omega_C - \varepsilon_0[(\eta + \nu + 2m_1)^2 - (\eta + \nu + 2m_2)^2] - \hbar\omega_{IO-W}$ and $\hbar\omega = (\mathcal{N}_2 - \mathcal{N}_1)\hbar\omega_C - \varepsilon_0[(\eta + \nu + 2m_1)^2 - (\eta + \nu + 2m_2)^2] + \hbar\omega_{IO-W}$, i.e., $\hbar\omega_3$ and $\hbar\omega_4$ of 111.455 (meV) and 133.830 (meV). Based on the two conditions of the two OD-MIOPRs in the GaAs-well material, we can see that the (3)/(4)-number OD-MIOPR peak describes the simultaneous absorption/emission of the energies of an IO-phonon in

the GaAs-well material ($\hbar\omega_{IO-W}$) and of an incident photon ($\hbar\omega$) by the Pöschl–Teller potential confinement electron to shift from $\mathcal{N}_1$ to $\mathcal{N}_2$ and m_1 to m_2 in the potential Pöschl–Teller GaAs/AlAs QW.

Our study has the main purpose is to compare the el–IO-ph interaction strength in the potential Pöschl–Teller GaAs/AlAs QW with that in the potential rectangular GaAs/AlAs QW in both the two absorption and emission cases of an IO-phonon not only in the GaAs-well material but also in the AlAs-barrier material of the two types of the quantum wells. Therefore, the MO properties are caused by the el–IO-ph interaction of the potential Pöschl–Teller GaAs/AlAs QW based on the characteristics of both the four OD-MIOPR peaks (from (2)-peak to (5)-peak) were studied in detail and compared with those of the rectangular GaAs/AlAs QW, as were shown in the figures below. Our specific results are expected to be promising data for potential applications in optoelectronic devices.

In Fig. 3, we plotted the $\hbar\omega$-dependent MOAP due to the el–IO-ph interaction at the four OD-MIOPR peaks in the two emission and absorption cases of an IO-phonon in the well GaAs-material (Figs. 3(b) and 3(c)) and barrier AlAs-material (Figs. 3(a) and 3(d)) of the Pöschl–Teller GaAs/AlAs QW. Where $B = 10$ T, $L_W = \sqrt{\frac{5}{3}} \times 12.65 \times 10^{-9}$ m, $\eta = \nu = 2$, and $T = 300$ K. To perform an important aim of this study as above mentioned, the characteristics of both the four OD-MIOPR peaks (from (2)-peak to (5)-peak) have to study in detail aimed at obtaining the MO properties are caused by the el–IO-ph interaction of the Pöschl–Teller GaAs/AlAs QW and compare with those of the rectangular GaAs/AlAs QW. Thus, these four specific OD-MIOPR peaks as indicated in Fig. 3 were separated from Fig. 2 for a reason that can be more evidently observed. Where Figs. 3(a) and 3(b) indicate respectively the two OD-MIOPR peaks in the barrier and the well along with an IO-phonon absorption. Figs. 3(c) and 3(d) indicate respectively the two OD-MIOPR peaks in the well and the barrier along with an IO-phonon emission.

In Figs. 4, 6, and 8 we plotted the $\hbar\omega$-dependent MOAP due to the el–IO-ph interaction with various values of the T (Fig. 4), the
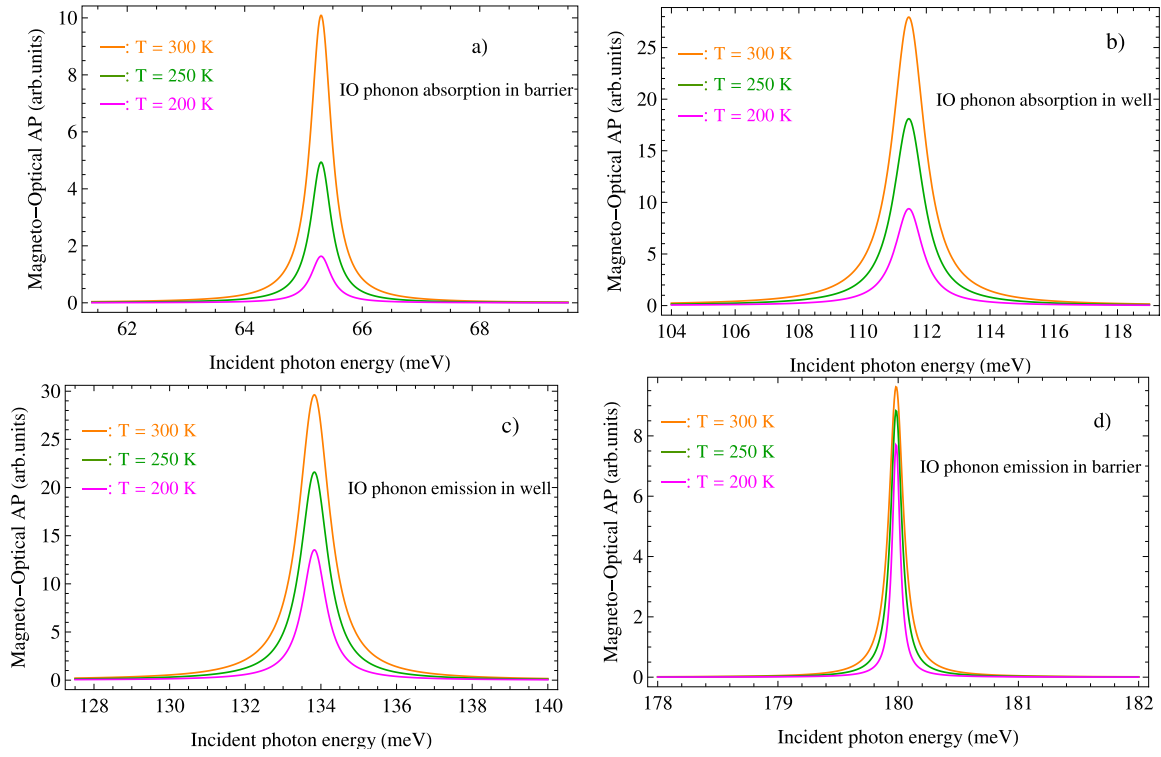
Fig. 4. Photon-energy dependent MOAP due to the el–IO-ph interaction with different T-values at the four OD-MIOPR peaks in the two emission and absorption cases of an IO-phonon in the well GaAs-material (Figs. 4(b) and 4(c)) and barrier AlAs-material (Figs. 4(a) and 4(d)) of the Pöschl–Teller GaAs/AlAs QW. Where $B = 10$ T, $L_W = \sqrt{\frac{5}{3}} \times 12.65 \times 10^{-9}$ m, and $\eta = \nu = 2$.
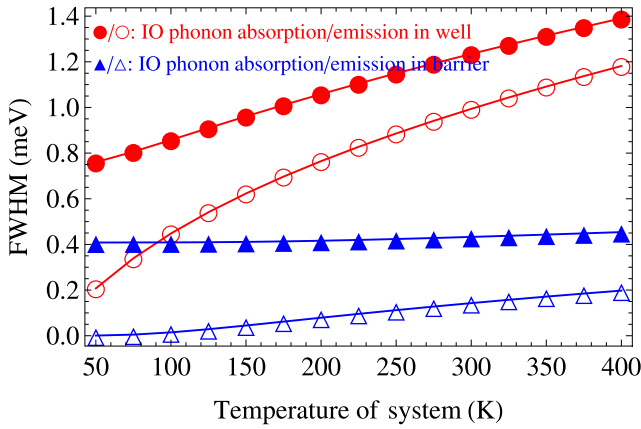

Fig. 5. T-dependent FWHM of the four OD-MIOPR peaks in the two emission and absorption cases of an IO-phonon in the well GaAs-material (the filled and empty red-circles) and barrier AlAs-material (the filled and empty blue-triangles) of the Pöschl–Teller GaAs/AlAs QW due to the el–IO-ph interaction. Where $B = 10$ T, $L_W = \sqrt{\frac{5}{3}} \times 12.65 \times 10^{-9}$ m, $\eta = \nu = 2$, and $T = 300$ K.

L_W (Fig. 6), and the B (Fig. 8) at the four OD-MIOPR peaks in the two emission and absorption cases of an IO-phonon in the well GaAs-material (figures (b) and (c)) and barrier AlAs-material (figures (a) and (d)) of the Pöschl–Teller GaAs/AlAs QW when $\eta = \nu = 2$. Where $B = 10$ T, $L_W = \sqrt{\frac{5}{3}} \times 12.65 \times 10^{-9}$ m, and the orange, green, and magenta curves refer to the $T = 300$ K, $T = 250$ K, and $T = 200$ K, respectively in Fig. 4 for both the four above OD-MIOPR peaks. In Fig. 6, $B = 10$ T, $T = 300$ K, and the orange, green, and magenta curves refer to the $L_W = \sqrt{\frac{5}{3}} \times 12.65 \times 10^{-9}$ m, $L_W = \sqrt{\frac{5}{3}} \times 11.65 \times 10^{-9}$ m, and $L_W = \sqrt{\frac{5}{3}} \times 10.65 \times 10^{-9}$ m respectively. Finally, $T = 300$ K,

$L_W = \sqrt{\frac{5}{3}} \times 12.65 \times 10^{-9}$ m, and the orange, green, and magenta curves refer to the $B = 10$ T, $B = 11$ T, and $B = 12$ T, respectively in Fig. 8 for both the four above OD-MIOPR peaks. From numerical calculations, it can be realized that the MOAP of the confinement electron in the potential Pöschl–Teller GaAs/AlAs QW at the OD-MIOPR peaks in the two emission and absorption cases of an IO-phonon in the GaAs (well) and the AlAs (barrier) increases in magnitude with the T (see in Fig. 4), the L_W (see in Fig. 6), and the B (see in Fig. 8). However, these OD-MIOPR-peaks' position has no change when changing T, but it has an evident red (blue) shift when changing L_W (B). The cause of these characteristics is as follows: The resonance-conditions of both the four OD-MIOPR peaks in the two emission and absorption cases of an IO-phonon in the GaAs (well) and the AlAs (barrier) of the Pöschl–Teller GaAs/AlAs QW due to the el–IO-ph interaction have no dependence on the T, as indicated by the two Eqs.: $\hbar\omega = (\mathcal{N}_2 - \mathcal{N}_1)\hbar\omega_C - \varepsilon_0[(\eta + \nu + 2m_1)^2 - (\eta + \nu + 2m_2)^2] \mp \hbar\omega_{IO-B}$ and $\hbar\omega = (\mathcal{N}_2 - \mathcal{N}_1)\hbar\omega_C - \varepsilon_0[(\eta + \nu + 2m_1)^2 - (\eta + \nu + 2m_2)^2] \mp \hbar\omega_{IO-W}$ of the OD-MIOPR peaks in the two absorption and emission cases of an IO-phonon in the barrier and the well, respectively. However, the T was included in both the n_q (distribution function of an IO-phonon) and the $f_{\mathcal{N},m}$ (distribution function of the Pöschl–Teller GaAs/AlAs QW electron) in the well GaAs-material and the barrier AlAs-material. Simultaneously, the MOAP of the confinement electron in the potential Pöschl–Teller GaAs/AlAs QW at the OD-MIOPR peaks in the two emission and absorption cases of an IO-phonon in the GaAs (well) and the AlAs (barrier) increases in magnitude with the T, as indicated in Fig. 4 also is reason of the enhanced el–IO-ph scattering possibility in both in the GaAs-well and the AlAs-barrier materials when T increases. Furthermore, the interpretation for the OD-MIOPR-peaks' position has no change when changing T, but it has a phenomenon of evident red (blue) shift when changing L_W (B), as indicated in Figs. 6 and 8 is that the four OD-MIOPR peaks are caused by the four following resonance-conditions $\hbar\omega = (\mathcal{N}_2 - \mathcal{N}_1)\hbar\omega_C - \varepsilon_0[(\eta + \nu + 2m_1)^2 - (\eta + \nu + 2m_2)^2] \mp \hbar\omega_{IO-B}$ and $\hbar\omega = (\mathcal{N}_2 - \mathcal{N}_1)\hbar\omega_C - \varepsilon_0[(\eta + \nu + 2m_1)^2 - (\eta + \nu + 2m_2)^2] \mp \hbar\omega_{IO-W}$
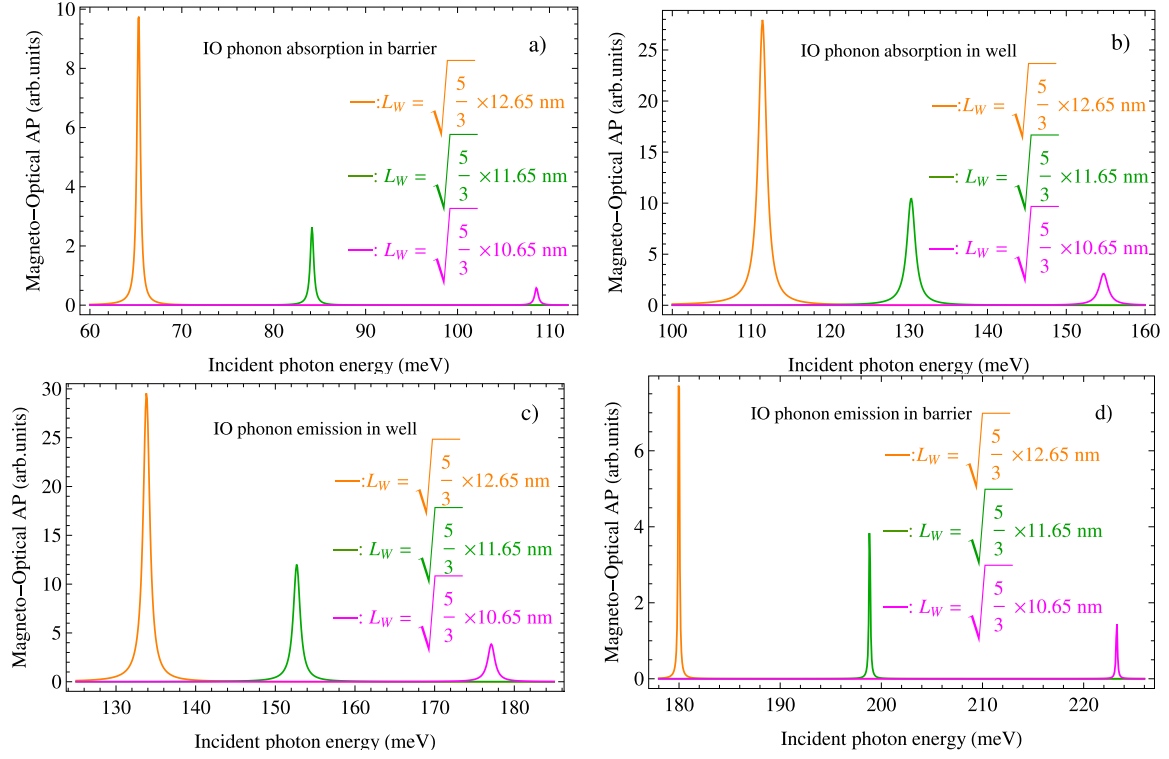
Fig. 6. Photon-energy dependent MOAP due to the el–IO-ph interaction with different L_W-values at the four OD-MIOPR peaks in the two emission and absorption cases of an IO-phonon in the well GaAs-material (Figs. 3(b) and 3(c)) and barrier AlAs-material (Figs. 3(a) and 3(d)) of the Pöschl–Teller GaAs/AlAs QW. Where $B = 10$ T, $\eta = \nu = 2$, and $T = 300$ K.

in the two emission and absorption cases of an IO-phonon in the GaAs (well) and the AlAs (barrier) of the potential Pöschl–Teller GaAs/AlAs QW due to the el–IO-ph interaction have an explicit dependence on both the L_W and B, as indicated by $\hbar\omega_C = \hbar|e|B/(cm^*)$ and $\varepsilon_0 = (\pi\hbar)^2/(8m^* L_W^2)$, respectively. Therefore, from the two expressions of $\hbar\omega_C = \hbar|e|B/(cm^*)$ and $\varepsilon_0 = (\pi\hbar)^2/(8m^* L_W^2)$, we easily understand that the enhanced photon energy with increasing B is for a reason that the enhanced $\hbar\omega_C$ with increasing B, and the reduced photon energy with increasing L_W is for a reason that the fast reduced $\hbar\omega_C$ with increasing L_W. Here is one of the main causes for the OD-MIOPR-peaks' position having a phenomenon of evident red (blue) shift when changing L_W (B). From obtained absorption-spectrum, it can be included that the L_W, T, and B strongly affect the MOAP of the confinement electron in the Pöschl–Teller GaAs/AlAs QW at the OD-MIOPR peaks in the two absorption and emission cases of an IO-phonon in both the GaAs-well and AlAs-barrier materials.

In Figs. 5, 7, and 9, we plotted T, L_W, and B-dependent FWHM of the four OD-MIOPR peaks in the two emission and absorption cases of an IO-phonon in the well GaAs-material (the filled and empty red-circles) and barrier AlAs-material (the filled and empty blue-triangles) of the Pöschl–Teller GaAs/AlAs QW due to the el–IO-ph interaction. Where $L_W = \sqrt{\frac{5}{3}} \times 12.65 \times 10^{-9}$ m, $\eta = \nu = 2$, and $B = 10$ T for Fig. 5; $B = 10$ T, $\eta = \nu = 2$, and $T = 300$ K for Fig. 7; finally $L_W = \sqrt{\frac{5}{3}} \times 12.65 \times 10^{-9}$ m, $\eta = \nu = 2$, and $T = 300$ K for Fig. 9. From the three Figs. 5, 7, and 9, we realize that the FWHM in the potential Pöschl–Teller GaAs/AlAs QW as a function of the T, L_W, and B at the OD-MIOPR peaks in the two absorption and emission cases of an IO-phonon in both the well and barrier. Namely, the FWHM of the OD-MIOPR peaks in the two emission and absorption cases of an IO-phonon in the GaAs (well) and AlAs (barrier) of the Pöschl–Teller potential is enhanced with T and B but diminished with L_W. The interpretation for this cause is that the enhanced el–IO-ph scattering possibility in the Pöschl–Teller GaAs/AlAs QW with increasing T or B, whereas the diminished el–IO-ph scattering possibility in the Pöschl–Teller GaAs/AlAs QW with
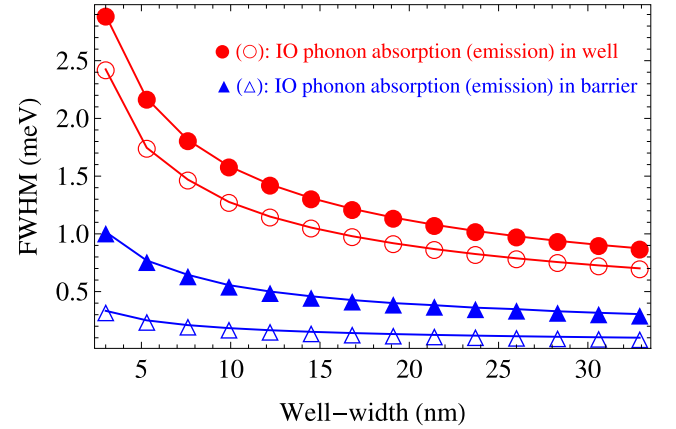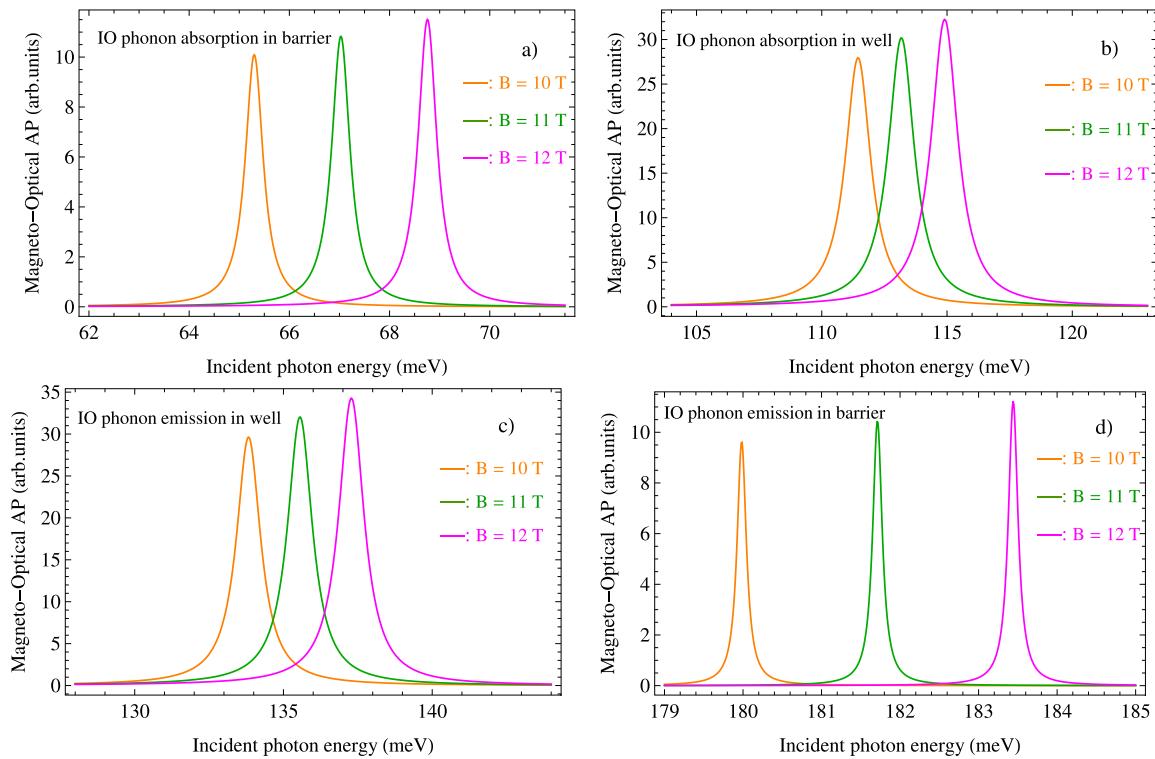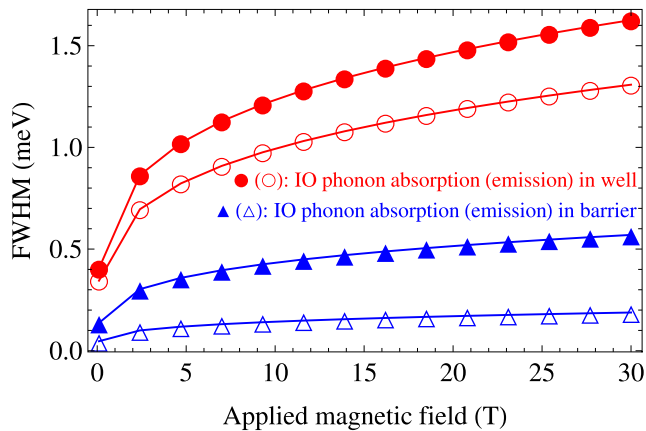

Fig. 7. L_W-dependent FWHM of the four OD-MIOPR peaks in the two emission and absorption cases of an IO-phonon in the well GaAs-material (the filled and empty red-circles) and barrier AlAs-material (the filled and empty blue-triangles) of the Pöschl–Teller GaAs/AlAs QW due to the el–IO-ph interaction. Where $B = 10$ T, $\eta = \nu = 2$, and $T = 300$ K.

increasing L_W. More importantly, T, L_W, and B-dependent FWHM of the four OD-MIOPR peaks in the two emission and absorption cases of an IO-phonon in the well GaAs- and barrier AlAs-materials of the potential Pöschl–Teller GaAs/AlAs QW due to the el–IO-ph interaction are qualitatively consistent with experimental observations [65–70]. In addition, we also realize that the FWHMs in both the well and barrier of the OD-MIOPR peaks in the absorption case of an IO-phonon always have larger values than do in the emission case of an IO-phonon. Concurrently, the FWHMs in the GaAs-well material always have larger values than do in the AlAs-barrier one for both the two emission and absorption cases of an IO-phonon of the OD-MIOPR peaks

Fig. 8. Photon-energy dependent MOAP due to the el–IO-ph interaction with different *B*-values at the four OD-MIOPR peaks in the two emission and absorption cases of an IO-phonon in the well GaAs-material (Figs. 3(b) and 3(c)) and barrier AlAs-material (Figs. 3(a) and 3(d)) of the Pöschl–Teller GaAs/AlAs QW. Where $L_W = \sqrt{\frac{5}{3}} \times 12.65 \times 10^{-9}$ m, $\eta = \nu = 2$, and $T = 300$ K.
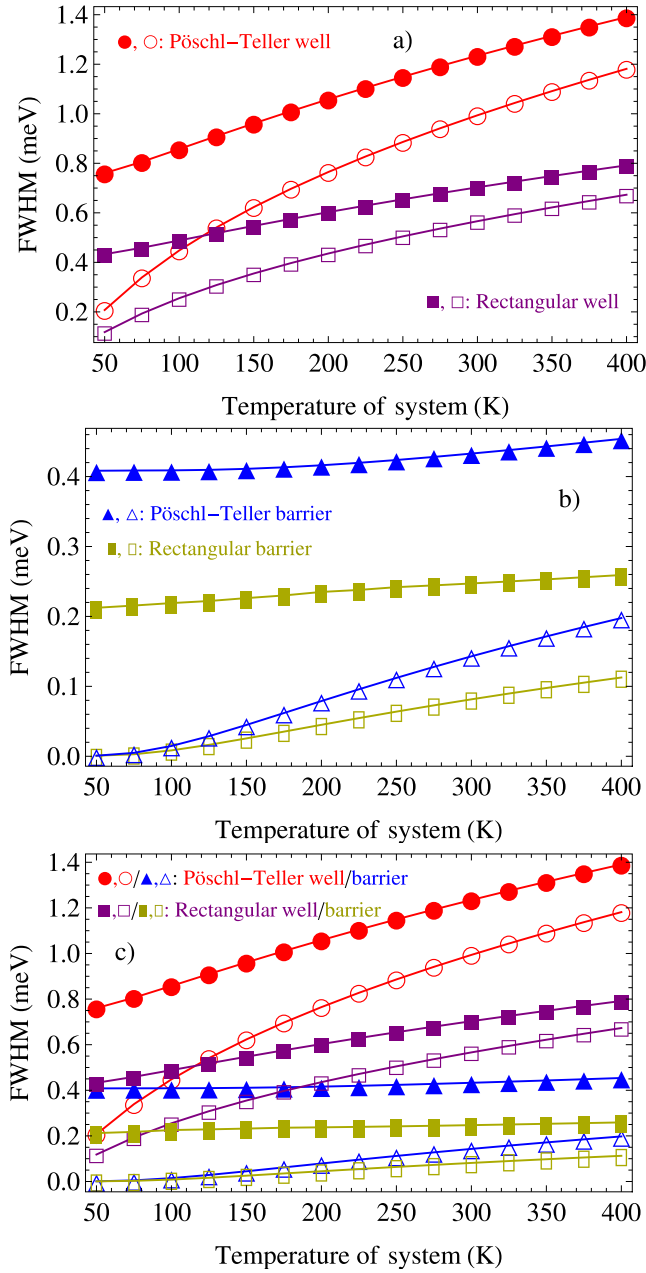

Fig. 9. *B*-dependent FWHM of the four OD-MIOPR peaks in the two emission and absorption cases of an IO-phonon in the well GaAs-material (the filled and empty red-circles) and barrier AlAs-material (the filled and empty blue-triangles) of the Pöschl–Teller GaAs/AlAs QW due to the el–IO-ph interaction. Where $L_W = \sqrt{\frac{5}{3}} \times 12.65 \times 10^{-9}$ m, $\eta = \nu = 2$, and $T = 300$ K.

in the potential Pöschl–Teller GaAs/AlAs QW. In other words, the *T*, L_W, and *B*-dependent FWHM in both the well and barrier of the OD-MIOPR peaks in the absorption case of an IO-phonon are stronger than those in the emission case of an IO-phonon. Simultaneously, the *T*, L_W, and *B*-dependent FWHM in the well GaAs-material always are stronger than those in the barrier AlAs-one in the two emission and absorption cases of an IO-phonon. A further important feature is that the electron interaction by the IO-phonon in the barrier is weaker than that in the well, however, its contribution is relatively significant wherefore the el–IO-ph interaction in barrier cannot be neglected when studying the el–IO-ph interaction in the potential Pöschl–Teller GaAs/AlAs QW.
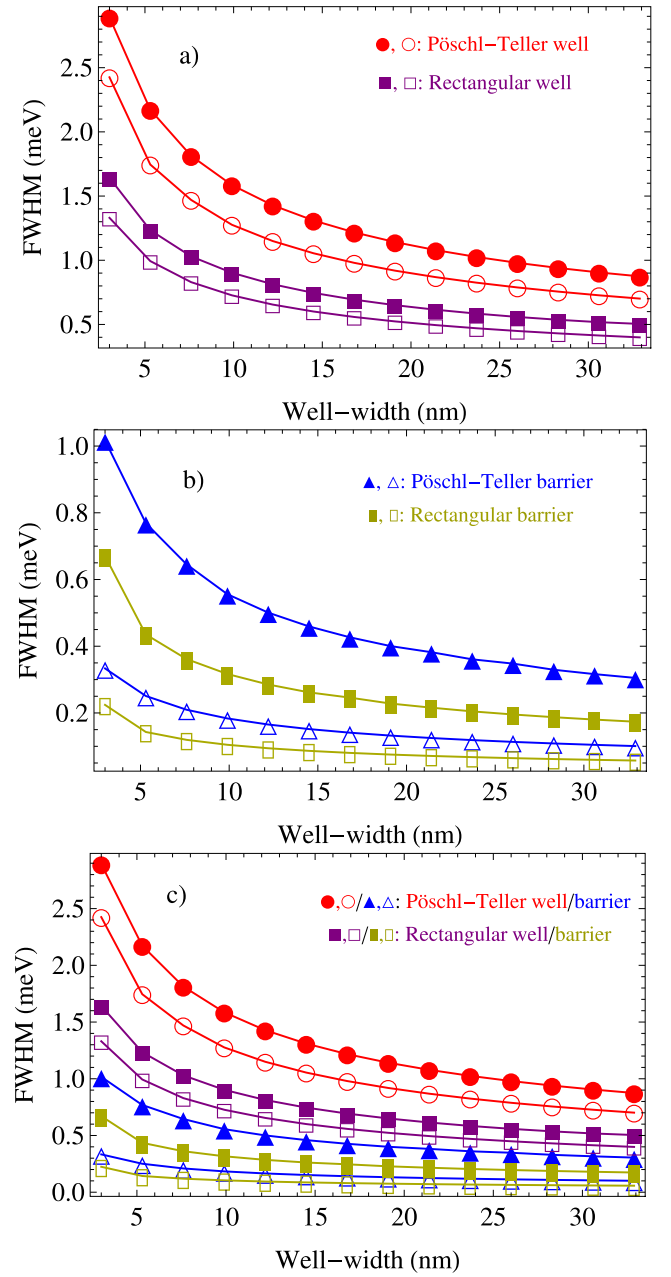
This is the L_W, *T*, and *B* strongly affect the FWHM of the OD-MIOPR peaks in the two emission and absorption cases of an IO-phonon in the GaAs (well) and AlAs (barrier). Therefore, the MO properties of the el–IO-ph interaction in the Pöschl–Teller GaAs/AlAs QW can be controlled/modified by changing the value of the L_W, *T*, and *B*. This characteristic will give a promising capacity for potential applications in optoelectronic devices.

Especially in the present work, a detailed comparison between the present results for the potential Pöschl–Teller GaAs/AlAs QW with the published ones for the potential rectangular GaAs/AlAs QWs have been presented. Namely, the comparison of the *T*, L_W, and *B*-dependent FWHM of the four OD-MIOPR peaks between the Pöschl–Teller and rectangular GaAs/AlAs QWs in both the two emission and absorption cases of an IO-phonon in the well GaAs-material (the filled and empty red circles, and the filled and empty purple squares) and barrier AlAs-material (the filled and empty blue triangles, and the filled and empty yellow rectangles), as shown in Figs. 10, 11, and 12. Where the parameter values are respectively taken as $L_W = \sqrt{\frac{5}{3}} \times 12.65 \times 10^{-9}$ m, $\eta = \nu = 2$, and $B = 10$ T for Fig. 10; $\eta = \nu = 2$, $B = 10$ T, and $T = 300$ K for Fig. 11; and $L_W = \sqrt{\frac{5}{3}} \times 12.65 \times 10^{-9}$ m, $\eta = \nu = 2$, and $T = 300$ K for Fig. 12. To clarify the difference in the MO-properties, especially FWHM, between the Pöschl–Teller and rectangular GaAs/AlAs QWs are caused by the e–IO-ph interaction in both the two absorption and emission cases of an IO-phonon not only in the well GaAs-material but also in the barrier AlAs-material, we have individually plotted for the well GaAs-material, barrier AlAs-material, and the combined well GaAs- and barrier AlAs-materials of GaAs and AlAs, as indicated respectively in Figs. (a), (b), and (c) of Figs. from 10–12. From obtained results in Figs. 10, 11, and 12, it can be remarked that the *T*, L_W, and *B*-dependent FWHM of the four OD-MIOPR peaks in both the two absorption and emission cases of an IO-phonon in the GaAs well-material and AlAs barrier-material of the potential Pöschl–Teller GaAs/AlAs QW are always stronger than those of the potential rectangular GaAs/AlAs QW. In other words, the FWHMs of the four OD-MIOPR peaks in both the two emission

Fig. 10. Comparison of the T-dependent FWHM of the four OD-MIOPR peaks between the Pöschl–Teller and rectangular GaAs/AlAs QWs in the two emission and absorption cases of an IO-phonon in the well GaAs-material (the filled and empty red-circles, and the filled and empty purple-squares) and barrier AlAs-material (the filled and empty blue-triangles, and the filled and empty yellow-rectangles). Where $B = 10$ T, $L_W = \sqrt{\frac{5}{3}} \times 12.65 \times 10^{-9}$ m, and $\eta = \nu = 2$.

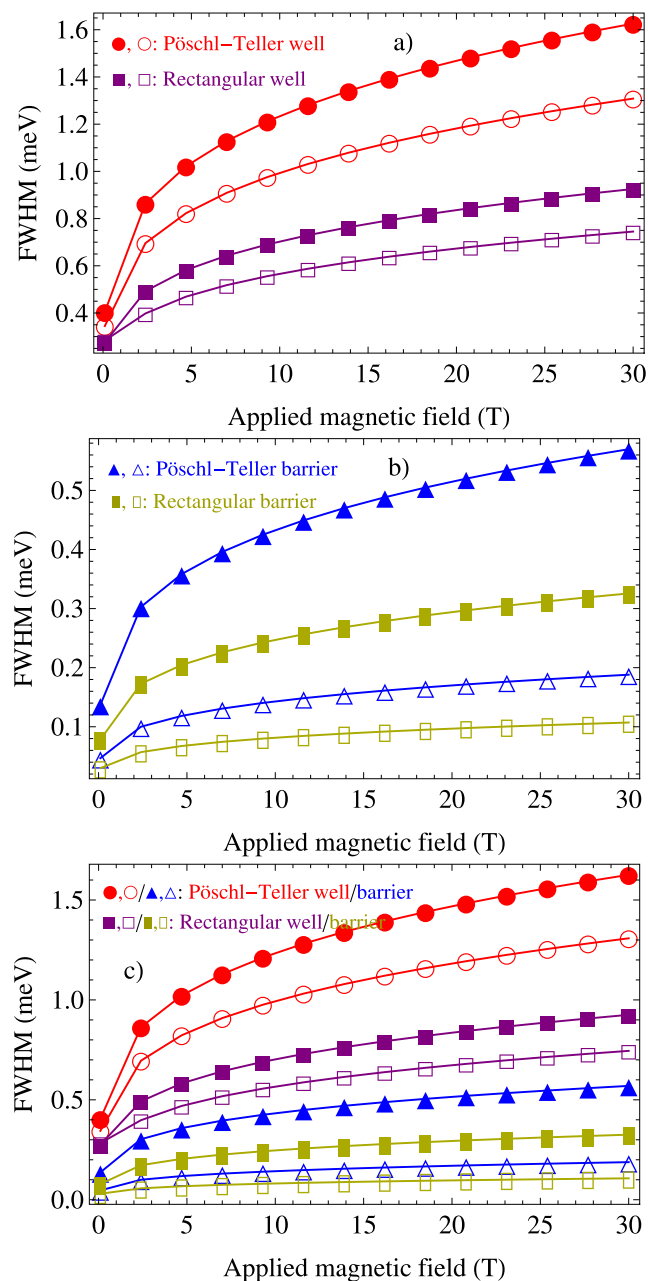**Fig. 11.** Comparison of the L_W-dependent FWHM of the four OD-MIOPR peaks between the Pöschl–Teller and rectangular GaAs/AlAs QWs in the two emission and absorption cases of an IO-phonon in the well GaAs-material (the filled and empty red-circles, and the filled and empty purple-squares) and barrier AlAs-material (the filled and empty blue-triangles, and the filled and empty yellow-rectangles). Where $B = 10$ T, $\eta = \nu = 2$, and $T = 300$ K.

and absorption cases of an IO-phonon in the well GaAs-material and barrier AlAs-material of the Pöschl–Teller GaAs/AlAs QW vary faster and have larger value than do of the rectangular GaAs/AlAs QW. This also gives a novel capacity for potential applications in optoelectronic devices. Simultaneously, in this comparison, we are easily seen that the T, L_W, and B-dependent FWHM of the OD-MIOPR peak in the absorption case of an IO-phonon in the GaAs well-material of the potential Pöschl–Teller GaAs/AlAs QW are the strongest, whereas the T, L_W, and B-dependent FWHM of the OD-MIOPR peak in the emission

case of an IO-phonon in the AlAs barrier-material of the rectangular GaAs/AlAs QW are the weakest.

5. Conclusions

We have reported in detail the MO-properties of the potential Pöschl–Teller GaAs-AlAs QW due to the el–IO-ph interaction for both the two emission and absorption cases of IO-phonons in the well GaAs- and barrier AlAs-materials by using the OD-MIOPR effect. Our results are found to be qualitatively consistent with observations by experiments. Simultaneously, the present results for the Pöschl–Teller

Fig. 12. Comparison of the B-dependent FWHM of the four OD-MIOPR peaks between the Pöschl–Teller and rectangular GaAs/AlAs QWs in the two emission and absorption cases of an IO-phonon in the well GaAs-material (the filled and empty red-circles, and the filled and empty purple-squares) and barrier AlAs-material (the filled and empty blue-triangles, and the filled and empty yellow-rectangles). Where $L_W = \sqrt{\frac{5}{3}} \times 12.65 \times 10^{-9}$ m, $\eta = \nu = 2$, and $T = 300$ K.

GaAs/AlAs QW also were compared with those for the rectangular QW which has been previously published in the Journal of Physica E [48]. The main results obtained from this work are as follows: For analytical calculations, we have obtained the explicit expression of the MOAP due to the el–IO-ph interaction in the Pöschl–Teller GaAs/AlAs QW for both the two emission and absorption cases of IO-phonons not only in the GaAs-well material but also in the AlAs-barrier material. Based on the analytical calculations, numerical calculations also were performed, and the results show that the MOAP of the confinement electron in the potential Pöschl–Teller GaAs/AlAs QW at the OD-MIOPR peaks in the two emission and absorption cases of IO-phonons in well and barrier increases in magnitude with the L_W, the T, and the B. However,

these OD-MIOPR-peaks' position has no change when changing T, but it has an evident red (blue) shift when changing L_W (B). Moreover, the FWHM of the OD-MIOPR peaks in the two emission and absorption cases of IO-phonons in the GaAs (well) and AlAs (barrier) materials of the Pöschl–Teller potential is enhanced with T and B but diminished with L_W. The FWHM of the OD-MIOPR peaks in the two emission and absorption cases of IO-phonons in the well and barrier of the potential Pöschl–Teller GaAs/AlAs QW strongly depend on the L_W, T, and B. In other words, the L_W, T, and B strongly affect the MOAP and the FWHM of the OD-MIOPR peaks in the two emission and absorption cases of IO-phonons in both the GaAs (well) and AlAs (barrier) materials. Therefore, the MO properties produced by the el–IO-ph interaction in the Pöschl–Teller GaAs/AlAs QW can be controlled/modified by changing the values of L_W, T, and B. This characteristic will give a promising capacity for potential applications in optoelectronic devices. In addition, the T, L_W, and B-dependent FWHM due to IO-phonon interaction in both the well and barrier of the OD-MIOPR peaks in the absorption case of an IO-phonon are stronger than those in the emission case of an IO-phonon. Besides, a further important feature found from this study is that the electron interaction by the IO-phonon in the barrier is weaker than that in the well, however, its contribution is relatively significant wherefore the el–IO-ph interaction in barrier cannot be neglected when studying the el–IO-ph interaction in the Pöschl–Teller GaAs/AlAs QW. In particular, our finding shows that the FWHMs due to IO-phonon interaction in the potential Pöschl–Teller QW are always bigger than those in the potential rectangular one for both the two emission and absorption cases of IO-phonons in the GaAs-well and AlAs-barrier materials. This demonstrates that the electron–interface optical phonon interaction strength in Pöschl–Teller quantum wells is enhanced considerably compared to rectangular ones.

CRediT authorship contribution statement

Nguyen Dinh Hien: Writing – review & editing, Writing – original draft, Visualization, Software, Resources, Methodology, Investigation.

Declaration of competing interest

The authors declare that they have no known competing financial interests or personal relationships that could have appeared to influence the work reported in this paper.

Data availability

Data will be made available on request.

References

[1] C.T. Giner, F. Comas, Electron–lo-phonon interaction in semiconductor double heterostructures, Phys. Rev. B 37 (1988) 4583–4588.
[2] N. Mori, T. Ando, Electron–optical-phonon interaction in single and double heterostructures, Phys. Rev. B 40 (1989) 6175–6188.
[3] B. Anasori, Y. Xie, M. Beidaghi, J. Lu, B.C. Hosler, L. Hultman, P.R.C. Kent, Y. Gogotsi, M.W. Barsoum, Two-dimensional, ordered, double transition metals carbides (mxenes), ACS Nano 9 (2015) 9507–9516, http://dx.doi.org/10.1021/acsnano.5b03591, pMID: 26208121.
[4] S. Guo, D. Yang, D. Wang, X. Fang, D. Fang, X. Chu, X. Yang, J. Tang, L. Liao, Z. Wei, Response improvement of gaas two-dimensional non-layered sheet photodetector through sulfur passivation and plasma treatment, Vacuum 197 (2022) 110792.
[5] M. Naguib, O. Mashtalir, J. Carle, V. Presser, J. Lu, L. Hultman, Y. Gogotsi, M.W. Barsoum, Two-dimensional transition metal carbides, ACS Nano 6 (2012) 1322–1331, http://dx.doi.org/10.1021/nn204153h, pMID: 22279971.
[6] M. Naguib, M. Kurtoglu, V. Presser, J. Lu, J. Niu, M. Heon, L. Hultman, Y. Gogotsi, M.W. Barsoum, Two-dimensional nanocrystals produced by exfoliation of ti3alc2, Adv. Mater. 23 (2011) 4248–4253, arXiv:https://onlinelibrary.wiley.com/doi/pdf/10.1002/adma.201102306.
[7] M. Naguib, J. Halim, J. Lu, K.M. Cook, L. Hultman, Y. Gogotsi, M.W. Barsoum, New two-dimensional niobium and vanadium carbides as promising materials for li-ion batteries, J. Am. Chem. Soc. 135 (2013) 15966–15969, http://dx.doi.org/10.1021/ja405735d, pMID: 24144164.

[8] V. Khranovskyy, A.M. Glushenkov, Y. Chen, A. Khalid, H. Zhang, L. Hultman, B. Monemar, R. Yakimova, Crystal phase engineered quantum wells in zno nanowires, Nanotechnology 24 (2013) 215202.

[9] V. Donchev, T. Ivanov, I. Ivanov, M. Angelov, K. Germanova, High-temperature excitons in gaas quantum wells embedded in alas/gaas superlattices, Vacuum 58 (2000) 478–484.

[10] Y.-S. Chen, C.-Y. Kao, K.-W. Lee, Y.-H. Wang, Fabrication and application of gaas-on-insulator structure prepared through liquid-phase chemical-enhanced oxidation, Vacuum 171 (2020) 109007.

[11] N. Shtinkov, V. Donchev, K. Germanova, S. Vlaev, I. Ivanov, Effect of non-abrupt interfaces in alas/gaas superlattices with embedded gaas quantum wells, Vacuum 58 (2000) 561–567.

[12] M. Wang, J. Zhu, Y. Zi, Z.-G. Wu, H. Hu, Z. Xie, Y. Zhang, L. Hu, W. Huang, Functional two-dimensional black phosphorus nanostructures towards next-generation devices, J. Mater. Chem. A 9 (2021) 12433–12473.

[13] Y. Zi, J. Zhu, L. Hu, M. Wang, W. Huang, Nanoengineering of tin monosulfide (sns)-based structures for emerging applications, Small Sci. 2 (2022) 2100098, arXiv:https://onlinelibrary.wiley.com/doi/pdf/10.1002/smsc.202100098.

[14] W. Huang, L. Hu, Y. Tang, Z. Xie, H. Zhang, Recent advances in functional 2d mxene-based nanostructures for next-generation devices, Adv. Funct. Mater. 30 (2020) 2005223, arXiv:https://onlinelibrary.wiley.com/doi/pdf/10.1002/adfm.202005223.

[15] W. Huang, Y. Zhang, Q. You, P. Huang, Y. Wang, Z.N. Huang, Y. Ge, L. Wu, Z. Dong, X. Dai, Y. Xiang, J. Li, X. Zhang, H. Zhang, Enhanced photodetection properties of tellurium@selenium roll-to-roll nanotube heterojunctions, Small 15 (2019) 1900902, arXiv:https://onlinelibrary.wiley.com/doi/pdf/10.1002/smll.201900902.

[16] C. Chen, M. Dutta, M.A. Stroscio, Confined and interface phonon modes in GaN/ZnO heterostructures, J. Appl. Phys. 95 (2004) 2540–2546, arXiv:https://pubs.aip.org/aip/jap/article-pdf/95/5/2540/10634367/2540_1_online.pdf.

[17] R. Zheng, M. Matsuura, Well-width dependence of electron–phonon interaction energies in quantum wells due to confined lo phonon modes, Phys. Rev. B 61 (2000) 12624–12627.

[18] N.D. Hien, Influence of four confinement phonon models on the electron self-energy in a finite-square potential quantum-well, Micro Nanostruct. 179 (2023) 207563.

[19] N.D. Hien, Effect of the electronic confinement potential on the electron–lo-phonon interaction energy in a quantum well, Phys. Scr. 98 (2023) 065940.

[20] S.M. Komirenko, K.W. Kim, M.A. Stroscio, M. Dutta, Energy-dependent electron scattering via interaction with optical phonons in wurtzite crystals and quantum wells, Phys. Rev. B 61 (2000) 2034–2040.

[21] S. Rudin, T.L. Reinecke, Electron–lo-phonon scattering rates in semiconductor quantum wells, Phys. Rev. B 41 (1990) 7713–7717.

[22] B.K. Ridley, Electron scattering by confined lo polar phonons in a quantum well, Phys. Rev. B 39 (1989) 5282–5286.

[23] M. Ziesmann, D. Heitmann, L.L. Chang, Interaction of optical phonons with electrons in an inas quantum well, Phys. Rev. B 35 (1987) 4541–4544.

[24] N.D. Hien, Cyclotron resonance linewidth due to electron scattering by five different phonon modes in semiparabolic quantum wells, J. Phys. Chem. Solids 167 (2022) 110757.

[25] K. Sun, H. Chang, C. Wang, T. Song, S. Wang, C. Lee, Raman and hot electron–neutral acceptor luminescence studies of electron-optical phonon interactions in gaas/alxga1-xas quantum wells, Solid State Commun. 115 (2000) 563–567.

[26] K. Doan Quoc, H. Nguyen Dinh, Influence of confined phonon for the different models in gaas quantum wells on the optically detected electrophonon resonance linewidth, Opt. Quantum Electron. 51 (2019) 116.

[27] D.J. Barnes, R.J. Nicholas, F.M. Peeters, X.-G. Wu, J.T. Devreese, J. Singleton, C.J.G.M. Langerak, J.J. Harris, C.T. Foxon, Observation of optically detected magnetophonon resonance, Phys. Rev. Lett. 66 (1991) 794–797.

[28] N. Mori, H. Momose, C. Hamaguchi, Magnetophonon resonances in quantum wires, Phys. Rev. B 45 (1992) 4536–4539.

[29] G.-Q. Hai, F.M. Peeters, Optically detected magnetophonon resonances in gaas, Phys. Rev. B 60 (1999) 16513–16518.

[30] S.Y. Choi, S.C. Lee, H.J. Lee, H.S. Ahn, S.W. Kim, J.Y. Ryu, Optically detected magnetophonon resonances in semiconductor based *n*-ge and *n*-gaas, Phys. Rev. B 66 (2002) 155208.

[31] S.C. Lee, H.S. Ahn, D.S. Kang, S.O. Lee, S.W. Kim, Optically detected magnetophonon resonances in n-ge in tilted magnetic fields, Phys. Rev. B 67 (2003) 115342.

[32] H.V. Phuc, N.D. Hien, L. Dinh, T.C. Phong, Confined optical-phonon-assisted cyclotron resonance in quantum wells via two-photon absorption process, Superlattices Microstruct. 94 (2016) 51–59.

[33] N.D. Hien, C.V. Nguyen, N.N. Hieu, S.S. Kubakaddi, C.A. Duque, M.E. Mora-Ramos, L. Dinh, T.N. Bich, H.V. Phuc, Magneto-optical transport properties of monolayer transition metal dichalcogenides, Phys. Rev. B 101 (2020) 045424.

[34] N.D. Hien, Magnetophonon resonance in quantum wells due to absorption and emission of confined phonon, Physica E 114 (2019) 113608.

[35] N.D. Hien, Influence of the confining potential on the linewidth of a quantum well, Superlattices Microstruct. 160 (2021) 107068.

[36] N.D. Hien, Comparison of the magneto-optical properties of the semi-parabolic well with those of the parabolic and rectangular wells under the combined influences of aluminum concentration and hydrostatic pressure, J. Phys. Chem. Solids (2021) 110456.

[37] N.D. Hien, Combined influences of temperature, pressure, and alloy-composition on magneto-optical properties of the semi-parabolic well under all four different phonon models, Micro Nanostruct. 167 (2022) 207236.

[38] N.D. Hien, Intersubband absorption linewidth in a semi-parabolic quantum well: Comparison among three different phonon models, Physica B 638 (2022) 413901.

[39] M.V. Klein, IEEE J. Quantum Electron. QE-22 (1986) 1760.

[40] R. Lassnig, Polar optical interface phonons and fröhlich interaction in double heterostructures, Phys. Rev. B 30 (1984) 7132–7137.

[41] Youcef A. Bioud, Abderraouf Boucherif, Ali Belarouci, Etienne Paradis, Dominique Drouin, Richard Arès, Chemical composition of nanoporous layer formed by electrochemical etching of p-type gaas, Nanoscale Res. Lett. 11 (2016) 1–8.

[42] V.A. Fonoberov, A.A. Balandin, Interface and confined optical phonons in wurtzite nanocrystals, Phys. Rev. B 70 (2004) 233205.

[43] J. j. Shi, Interface optical-phonon modes and electron–interface-phonon interactions in wurtzite gan/aln quantum wells, Phys. Rev. B 68 (2003) 165335.

[44] L. Zhang, J. j. Shi, T.L. Tansley, Polar vibration spectra of interface optical phonons and electron-interface optical phonon interactions in a wurtzite gan-aln nanowire, Phys. Rev. B 71 (2005) 245324.

[45] S.-F. Ren, H. Chu, Y.-C. Chang, Anisotropy of optical phonons and interface modes in gaas-alas superlattices, Phys. Rev. B 37 (1988) 8899–8911.

[46] J. j. Shi, S. h. Pan, Electron–interface-phonon interaction and scattering in asymmetric semiconductor quantum-well structures, Phys. Rev. B 51 (1995) 17681–17688.

[47] J.S. Bhat, B.G. Mulimani, S.S. Kubakaddi, Free carrier absorption in quantum well structures due to confined and interface optical phonons, Phys. Status Solidi (b) 182 (1994) 119–131, arXiv:https://onlinelibrary.wiley.com/doi/pdf/10.1002/pssb.2221820112.

[48] H.K. Dan, L. Dinh, H.D. Trien, T.C. Phong, N.D. Hien, Electron–interface phonon scattering in quantum wells due to absorbtion and emission of interface phonons, Physica E 120 (2020) 114043.

[49] L.T. Quynh Huong, L.N. Minh, L. Dinh, N.D. Hien, Cyclotron–interface phonon resonance line-width in asymmetric semiparabolic quantum wells, J. Phys. Chem. Solids 152 (2021) 109967.

[50] N.D. Vy, L.N. Minh, N.D. Hien, Influence of interface modes compared to confined modes on phonon-assisted cyclotron resonance effect in quantum wells, Superlattices Microstruct. 145 (2020) 106630.

[51] N.D. Hien, Comparison of the contribution of different types of interface-optical phonon modes to electron–phonon scattering in a quasi-two-dimensional system, Physica B 621 (2021) 413317.

[52] H. Yıldır ım, M. Tomak, Nonlinear optical properties of a pöschl-teller quantum well, Phys. Rev. B 72 (2005) 115340.

[53] S. Şakiroğlu, F. Ungan, U. Yesilgul, M. Mora-Ramos, C. Duque, E. Kasapoglu, H. Sari, Sökmen, Nonlinear optical rectification and the second and third harmonic generation in pöschl–teller quantum well under the intense laser field, Phys. Lett. A 376 (2012) 1875–1880.

[54] K.D. Pham, L.V. Tung, D.V. Thuan, C.V. Nguyen, N.N. Hieu, H.V. Phuc, Phonon-assisted cyclotron resonance in pöschl-teller quantum well, J. Appl. Phys. 126 (2019) 124301, http://dx.doi.org/10.1063/1.5103187.

[55] H. Yildirim, M. Tomak, Intensity-dependent refractive index of a pöschl-teller quantum well, J. Appl. Phys. 99 (2006) 093103, http://dx.doi.org/10.1063/1.2194124.

[56] N.D. Hien, Optical properties of a single quantum well with pöschl–teller confinement potential, Physica E 145 (2023) 115504.

[57] R. Lassnig, Polar optical interface phonons and fröhlich interaction in double heterostructures, Phys. Rev. B 30 (1984) 7132–7137.

[58] J.S. Bhat, B.G. Mulimani, S.S. Kubakaddi, Localized phonon-assisted cyclotron resonance in gaas/alas quantum wells, Phys. Rev. B 49 (1994) 16459–16466.

[59] N.L. Kang, S.D. Choi, Y.J. Cho, A many-body theory of quantum-limit cyclotron transition line-shapes in electron-phonon systems based on projection technique, Progr. Theoret. Phys. 96 (1996) 307–316, arXiv:http://oup.prod.sis.lan/ptp/article-pdf/96/2/307/5246478/96-2-307.pdf.

[60] N. Lyong Kang, J.H. Lee, D.-S. Choi, Calculation of cyclotron resonance linewidths in ge by using a many-body state-independent projection technique, J. Korean Phys. Soc. 37 (2000) 339–342.

[61] J. Yon Ryu, S. Choon Chung, Comparison of two techniques in the theory of phonon-induced cyclotron resonance line shapes, Phys. Rev. B 32 (1985) 7769–7775.

[62] J.Y. Sug, S.G. Jo, J. Kim, J.H. Lee, S.D. Choi, Quantum transition processes in deformation potential interacting systems using the equilibrium density projection technique, Phys. Rev. B 64 (2001) 235210.

[63] M.P. Chaubey, C.M. Van Vliet, Transverse magnetoconductivity of quasi-two-dimensional semiconductor layers in the presence of phonon scattering, Phys. Rev. B 33 (1986) 5617–5622.

[64] S. Adachi, Gaas, alas, And algaas: Material parameters for use in research and device applications, J. Appl. Phys. 58 (1985) R1–R29, http://dx.doi.org/10.1063/1.336070.

[65] M. Singh, Cyclotron-resonance linewidth due to electron–phonon interaction in multi-quantum-well structures, Phys. Rev. B 35 (1987) 9301–9304.

[66] T. Unuma, M. Yoshita, T. Noda, H. Sakaki, H. Akiyama, Intersubband absorption linewidth in gaas quantum wells due to scattering by interface roughness, phonons, alloy disorder, and impurities, J. Appl. Phys. 93 (2003) 1586–1597, http://dx.doi.org/10.1063/1.1535733.

[67] T. Unuma, T. Takahashi, T. Noda, M. Yoshita, H. Sakaki, M. Baba, H. Akiyama, Effects of interface roughness and phonon scattering on intersubband absorption linewidth in a gaas quantum well, Appl. Phys. Lett. 78 (2001) 3448–3450, http://dx.doi.org/10.1063/1.1376154.

[68] Y. Gu, Y.G. Zhang, X.Y. Chen, S.P. Xi, B. Du, Y.J. Ma, Effect of bismuth surfactant on inp-based highly strained inas/ingaas triangular quantum wells, Appl. Phys. Lett. 107 (2015) 212104, http://dx.doi.org/10.1063/1.4936379.

[69] K.L. Campman, H. Schmidt, A. Imamoglu, A.C. Gossard, Interface roughness and alloy-disorder scattering contributions to intersubband transition linewidths, Appl. Phys. Lett. 69 (1996) 2554–2556, http://dx.doi.org/10.1063/1.117737.

[70] M. Belmoubarik, K. Ohtani, H. Ohno, Intersubband transitions in zno multiple quantum wells, Appl. Phys. Lett. 92 (2008) 191906, http://dx.doi.org/10.1063/1.2926673.